UNCLASSIFIED

TARDEC

--- TECHNICAL REPORT ---

THE NATIONS'S LABORATORY FOR ADVANCED AUTOMOTIVE TECHNOLOGY

No.

Characterization of Borosilicate Glass Through Confined Compression Testing with Numerical Validation

Contract: W56HZV-06-C-0194
SwRI Report 18.12544/010

Prepared for
U.S. Army RDECOM-TARDEC
AMSRD-TAR-R
Warren, MI 48397-5000

November 2009

WINNER OF THE 1995 PRESIDENTIAL AWARD FOR QUALITY

DISTRIBUTION STATEMENT
Distribution A: Approved For Public Release; Distribution Unlimited.

U.S. Army Tank Automotive Research,
Development, and Engineering Center
Detroit Arsenal
Warren, Michigan 48397-5000

UNCLASSIFIED

Characterization of Borosilicate Glass Through Confined Compression Testing with Numerical Validation

Sidney Chocron
Charles E. Anderson, Jr.
Kathryn A. Dannemann
Arthur E. Nicholls

Southwest Research Institute®
P.O. Drawer 28510
San Antonio, TX 78238

Contract: W56HZV-06-C-0194

SwRI® Report 18.12544/010

Prepared for:

US Army RDECOM-TARDEC
AMSRD-TAR-R
Warren, MI 43897-5000

November 2009

REPORT DOCUMENTATION PAGE	*Form Approved* OMB No. 0704-0188

Public reporting burden for this collection of information is estimated to average 1 hour per response, including the time for reviewing instructions, searching data sources, gathering and maintaining the data needed, and completing and reviewing the collection of information. Send comments regarding this burden estimate or any other aspect of this collection of information, including suggestions for reducing this burden to Washington Headquarters Service, Directorate for Information Operations and Reports, 1215 Jefferson Davis Highway, Suite 1204, Arlington, VA 22202-4302, and to the Office of Management and Budget, Paperwork Reduction Project (0704-0188) Washington, DC 20503.

PLEASE DO NOT RETURN YOUR FORM TO THE ABOVE ADDRESS.

1. REPORT DATE *(DD-MM-YYYY)* 6-11-2009	**2. REPORT TYPE** Technical	**3. DATES COVERED** *(From - To)* April 2008 – November 2009

4. TITLE AND SUBTITLE Characterization of Borosilicate Glass Through Confined Compression Testing with Numerical Validation	**5a. CONTRACT NUMBER** W56HZV-06-C-0194
	5b. GRANT NUMBER
	5c. PROGRAM ELEMENT NUMBER
6. AUTHOR(S) Sidney Chocron, Charles E. Anderson, Jr. Kathryn A. Dannemann, and Arthur E. Nicholls	**5d. PROJECT NUMBER** 18.12544
	5e. TASK NUMBER
	5f. WORK UNIT NUMBER
7. PERFORMING ORGANIZATION NAME(S) AND ADDRESS(ES) Southwest Research Institute, P.O. Drawer 28510, San Antonio, TX 78238	**8. PERFORMING ORGANIZATION REPORT NUMBER** 18.12544/010
9. SPONSORING/MONITORING AGENCY NAME(S) AND ADDRESS(ES) US Army Tank-Automotive Research, Development, and Engineering Center, Warren, MI 48397-5000	**10. SPONSOR/MONITOR'S ACRONYM(S)** RDECOM-TARDEC
	11. SPONSORING/MONITORING AGENCY REPORT NUMBER

12. DISTRIBUTION AVAILABILITY STATEMENT

Approved for Public Release; Unlimited Distribution

13. SUPPLEMENTARY NOTES

The views, opinion, and/or findings contained in this report are those of the authors and should not be construed as an official Department of the Army position, policy, or decision, unless so designated by other documents.

14. ABSTRACT

This report describes two different techniques utilized to characterize intact and damaged borosilicate glass at pressures up to 2 GPa: triaxial compression and confined sleeve. The results of the characterization experiments—for intact and damaged glass as a function of confinement pressure—are described; the results are interpreted in terms of two pressure-dependent constitutive models: Drucker-Prager and Mohr-Columb. Both constitutive models predict correctly the stress-strain response in numerical simulations of the experiments. The Mohr-Coulomb is successful at predicting the damage pattern. An observation is that the slopes of the two models appears to be independent of the degree of damage (intact, predamaged and severely damaged specimens). The two models are then used to compute the penetration velocity of a gold rod into borosilicate glass as a function of impact velocity. From the penetration experiments it was found that the Drucker-Prager and Mohr-Coulomb models required a cap, and low values of the intercepts (zero-pressure values) to replicate the experiments.

15. SUBJECT TERMS

borosilicate glass, Mohr-Columb, Drucker-Prager, constitutive modeling, characterization, numerical simulations, ballistic experiments, damage, triaxial compression, confined sleeve

16. SECURITY CLASSIFICATION OF: Unclassified, Unlimited Distribution			**17. LIMITATION OF ABSTRACT**	**18. NUMBER OF PAGES**	**19a. NAME OF RESPONSIBLE PERSON** Dr. Douglas Templeton
a. REPORT Unlimited	**b. ABSTRACT** Unlimited	**c. THIS PAGE** Unlimited	None	54	**19b. TELEPONE NUMBER (*Include area code)*** 586-574-5325

Table of Contents

Page

1.0 Introduction 1
2.0 Experimental Technique 3
  2.1 Materials 3
  2.2 “Hydraulic Bomb” Technique 3
  2.3 “Confined Sleeve” Technique 5
3.0 Results and Interpretation 7
  3.1 Interpretation of the Hydraulic Bomb Experiments 7
    3.1.1 Intact Specimens 7
    3.1.2 Predamaged Specimens 8
  3.2 Interpretation of the Confined Sleeve Experiments 8
    3.2.1 Intact Specimens 8
    3.2.2 Predamaged Specimens 9
4.0 Constitutive Model Parameters 11
  4.1 Constitutive Models 11
    4.1.1 Drucker-Prager Model 11
    4.1.2 Mohr-Coulomb Model 11
  4.2 Hydraulic Bomb Tests Results 12
    4.2.1 Drucker-Prager Analysis 12
    4.2.1.1 Intact Specimens 12
    4.2.1.2 Predamaged Specimens 12
    4.2.2 Mohr-Coulomb Analysis 14
    4.2.2.1 Intact Specimens 14
    4.2.2.2 Predamaged Specimens 15
  4.3 Confined Sleeve Tests Results 17
    4.3.1 Drucker-Prager Analysis 17
    4.3.2 Mohr-Coulomb Analysis 18
  4.4 Summary of Constitutive Model Results 18
5.0 Numerical Simulations of Characterization Tests 21
  5.1 Introduction 21
  5.2 LS-DYNA Simulations of the Characterization Tests 21
    5.2.1 Hydraulic Bomb Tests 21
    5.2.2 Sleeve Tests – Static 23
    5.2.3 Sleeve Tests – Dynamic 23
6.0 Numerical Simulations of Reverse Ballistic Experiments 27
  6.1 Introduction 27

Table of Contents (Cont'd)

Page

- 6.2 Implementation of the Mohr-Coulomb Model in CTH 28
  - 6.2.1 Introduction 28
  - 6.2.2 Flow Surface and Implementation 28
- 6.3 Long-Rod Penetration Simulations 30
  - 6.3.1 Introduction 30
  - 6.3.2 Drucker-Prager Model 30
  - 6.3.3 Mohr-Coulomb Model 32

7.0 Characterization Data and Flyer-Plate Impact Data 35
- 7.1 Introduction 35
- 7.2 Plate Impact Experiments 35
- 7.3 Comparison of Characterization Experiments with Flyer-Plate Impact Experiments 38
  - 7.3.1 Confined Compression Tests on Intact Borosilicate Glass 38
  - 7.3.2 Predamaged Compression Tests on Borosilicate Glass 39
  - 7.3.3 Mohr-Coulomb Representation 40

8.0 Summary 41

9.0 Acknowledgement 43

10.0 References 45

List of Figures

Page

Figure 1. Hydraulic bomb experimental set-up 4

Figure 2. Specimen placement before being inserted into the pressure vessel 4

Figure 3. Confined sleeve test placed in the split-Hopkinson bar 5

Figure 4. Two intact specimens (BF-61 and BF-63) and two predamaged specimens (BF-49 and BF-53) tested in the bomb at 250 and 400 MPa nominal confinement pressures 7

Figure 5. Stress vs. strain for an initially intact specimen in a confined sleeve test under monotonic load (test BF-17) 8

Figure 6. Stress vs. sleeve hoop strain for an initially intact specimen in a confined sleeve test under monotonic load (test BF-17) 9

Figure 7. Equivalent stress vs. pressure for a predamaged specimen in a confined sleeve test under cyclic loading (test BF-14) 10

Figure 8. Interpretation of the sleeve tests with predamaged specimens 10

Figure 9. Equivalent stress at failure for different intact specimens tested in the hydraulic bomb 12

Figure 10. Equivalent stress at failure for different predamaged specimens tested in the bomb; unconfined tests are at the lower left 13

Figure 11. Residual equivalent stress for specimens tested in the hydraulic bomb 14

Figure 12. Two predamaged specimens that were tested in the bomb at 250 and 400 MPa confinement pressure. Shear angles were very similar for the whole range of confinement pressures, from 25 to 400 MPa 14

Figure 13. MC failure points for intact specimens tested in the bomb. σ_1 and σ_3 are the maximum and minimum principal stresses respectively 15

Figure 14. MC failure points for the damaged specimens tested in the bomb 16

Figure 15. MC residual strength data for predamaged specimens tested in the bomb 16

List of Figures (Cont'd)

Page

Figure 16. DP constitutive models inferred for intact and predamaged specimens 17

Figure 17. MC constitutive models inferred for intact and predamaged specimens 18

Figure 18. The failure of a predamaged specimen tested in the bomb at 400 MPa radial confining pressure is compared to specimen simulated with DYNA 22

Figure 19. Stress strain curves computed with LS-DYNA using the MC model are compared to test data 22

Figure 20. Test BF-14. Failure pattern for a predamaged specimen tested in the sleeve (left). Failure pattern obtained with the MC model in LS-DYNA (right) 23

Figure 21. Mesh and materials for the LS-DYNA model of the split-Hopkinson bar 24

Figure 22. Signal recorded by a strain gage placed on the input bar for two experiments (BF-75 and BF-77) and for the numerical simulation 24

Figure 23. Signal recorded by a strain gage placed on the output bar for two experiments (BF-75 and BF-77) and for the numerical simulation 25

Figure 24. Signal recorded by a strain gage placed on the sleeve for two experiments (BF-75 and BF-77) and for the numerical simulation 25

Figure 25. Signal recorded by a strain gage placed on the confining sleeve for two experiments (BF-75 and BF-77) and for the numerical simulation 26

Figure 26. Penetration and consumption velocities vs. impact velocity for borosilicate glass impacted by gold rods (regression lines recalculated to include highest velocity data points) 27

Figure 27. Implementation of Mohr-Coulomb model into CTH 29

Figure 28. The dependence of the penetration velocity on Y_{cap} 30

Figure 29. Sensitivity study on Y_0 (with $\beta = 1.2$ and $Y_{cap} = 1.78$ GPa) 31

Figure 30. Comparison of the simulation results to position-time data ($Y_0 = 25$ MPa) 32

Figure 31. The dependence of the penetration velocity on τ_{cap} 33

Figure 32. Sensitivity study on c (with $\mu = 0.6$ and $\tau_{cap} = 0.925$ GPa) 34

List of Figures (Cont'd)

Page

Figure 33. Equivalent stress vs. hydrostatic pressure for flyer-plate impact 35

Figure 34. Equivalent stress vs. hydrostatic pressure for flyer-plate impact experiments with adjusted HEL for Borofloat 37

Figure 35. Comparison of intact characterization data with flyer-plate impact data 38

Figure 36. Comparison of predamaged characterization data with flyer-plate impact experiments...39

Figure 37. Mohr-Coulomb representation of a comparison of characterization experiments and flyer-plate impact experiments...40

List of Tables

Page

Table 1. Mechanical Properties for Borofloat®33 3

Table 2. DP Parameters for Intact and Predamaged Borosilicate Glass ($Y = Y_0 + \beta P$) 19

Table 3. MC Parameters for Intact and Predamaged Specimens ($\tau = c + \mu \tilde{\sigma}_n$) 19

Table 4. MC Parameters Used in LS-DYNA Simulations for Predamaged Specimens 22

1.0 Introduction

Southwest Research Institute is involved in a multi-year program to characterize borosilicate glass. The main activities during this project included, but were not limited to:

- Impact (reverse ballistic) experiments of a gold long rod into intact borosilicate glass specimens at impact velocities from 0.4 km/s to 2.8 km/s [1]. Very high-speed digital imaging and flash radiography were used to measure the nose position and rod length as a function of time, and high-speed photography was used to measure the position of the failure front as a function of time. It was found that the failure front, which propagates at a speed much faster than the penetrating rod, quickly outdistances the projectile-target interface. Thus, except for the first few moments after impact, the rod presumably penetrates failed glass.
- Laboratory characterization of borosilicate glass at high pressures by performing compression tests under confinement. Specifically, predamaged and intact specimens were tested by two methods: triaxial compression and confined sleeve. The experiments were analyzed and interpreted using two pressure-dependent constitutive models—Drucker-Prager and Mohr-Coulomb—and constants for the two models were derived from the results of the laboratory experiments.
- Numerical simulations of the characterization tests and the ballistic tests to check the fidelity and the applicability of the derived constitutive models for representing the penetration response of borosilicate glass.

This report focuses on the last two items but uses the results from the first bullet. Triaxial compression (or confined compression) is a fairly well established technique to characterize, for example, geologic materials, see Desai and Siriwardane [2]. This technique allows a straightforward determination of Drucker-Prager or Mohr-Coulomb plasticity models. This is the first time, to the authors' knowledge, that the methods have been used to characterize borosilicate glass at high pressures.

The sleeve technique, i.e., confining the specimen with a thick steel sleeve, has also been used in the past to determine pressure dependence of the yield strength. For example, Chen and Ravichandran [3, 4] characterized ceramics at high strain rates and high pressures by confining them in metallic sleeves. Also, Ma and Ravi-Chandar [5], and Lu and Ravichandran [6], characterized aluminum and a metallic glass, respectively, at slow strain rates. More recently Chen and Luo [7] characterized intact and damaged ceramics under low confinement pressures at high strain rates. A confinement sleeve was also used by Forquin, *et al.* [8], in combination with numerical simulations, to characterize concrete at high pressures. In general, the above references confine the specimens at low to moderate pressures (100-300 MPa). In the present work, confinement pressures achieved—on the order of 1 GPa—are significantly higher. We also performed a limited number of tests at high strain rates and the results, validated with simulations, are presented.

Triaxial compression and confining sleeve techniques are complementary since one explores lower pressures than the other. The fact that they overlap at confining pressures of 300 to 400 MPa increases the confidence in the interpretation of the confining sleeve technique. Also, the high pressures achieved in the tests allow comparison of results with flyer-plate impact tests.

Flyer-plate impact experiments interrogate material response at very high strain rates, and thus, the comparison can provide insight to strain-rate effects. As will be discussed the comparisons of our data with Bourne, *et al*. [9], and with Alexander, *et al.* [10], give mixed results.

2.0 Experimental Technique

2.1 Materials

The characterization tests discussed below were performed on both intact and predamaged specimens of borosilicate glass. The brand name is Borofloat® 33, which is manufactured by Schott Glass using a float process. The X-ray fluorescence analysis performed on the test samples [11] indicates an approximate composition (by weight) of: 80.5 SiO_2, 12.7 B_2O_3, 2.5 Al_2O_3, 3.5 Na_2O, 0.64 K_2O. The elastic mechanical properties of Borofloat 33 were determined by ultrasound measurements [11] and are shown in Table 1. In Table 1, the symbols denote, respectively, density ρ, elastic modulus E, Poisson's ratio ν, the longitudinal sound speed c_L, and the shear wave speed c_s.

Table 1. Mechanical Properties for Borofloat®33

ρ (g/cm^3)	E (GPa)	ν (-)	c_L (km/s)	c_s (km/s)
2.22	62.3	0.20	5.61	3.41

2.2 "Hydraulic Bomb" Technique

The triaxial compression test is a "classic" test used to characterize pressure-dependent materials like sands or concrete, for example, see Ref. [2]. A specimen is placed inside a thick-wall steel pressure vessel (the pressure "bomb"). The pressure bomb is placed in an MTS machine. A steel piston runs from the loading platen of the MTS machine to the specimen through an alumina-loading anvil.[1] A hydraulic fluid, controlled by a pump, is used to load the specimen at different constant fluid pressures. An axial load is applied from the MTS machine. For simplicity, this test will be referred as "the bomb technique," or "hydraulic bomb," in the text.

Both intact and predamaged specimens were tested in compression inside a pressure vessel. The intact glass specimen is a cylinder with radius 3.175 mm and length 12 mm. The predamaged specimen was obtained by exposing the intact specimen to two cycles of 500° C in a furnace and suddenly placing the specimen into ice water. The predamaged specimens have non-contiguous cracks, but have strength (structural integrity) and can be handled readily without disintegrating into pieces. Dimensions (measured with a caliper) remain unchanged from the intact specimen [12].

The bomb set-up is illustrated in Fig. 1. The intact or predamaged specimens are introduced in a pressure vessel where they are loaded by a piston through two alumina anvils. The specimen is placed inside a pliable plastic (shrink tubing) sleeve to protect the specimen from the hydraulic fluid. The load is measured by a load cell placed inside the pressure vessel and wired directly to provide the equivalent stress acting on the specimen. For this simple load configuration with cylindrical symmetry the equivalent stress is:

$$\sigma_{eq} = |\sigma_z - \sigma_r| = \tilde{\sigma}_z - \tilde{\sigma}_r \tag{1}$$

---

[1] Tapered alumina anvils were used to load the specimen in compression. The alumina material has a nominal elastic modulus of 350 GPa and a compressive strength of 2 GPa (as reported by CoorsTek).

where σ_z is the axial load applied through the piston and σ_r is the fluid pressure ($\sigma < 0$ in compression, $\tilde{\sigma} > 0$ in compression).

Figure 2 shows the specimen, the anvils and the load cell before being placed inside the pressure vessel. The maximum pressure reachable in the vessel is 400 MPa due to limitations of the hydraulic pump. Tests were performed at fluid pressures of 25, 50, 100, 250, and 400 MPa. During a preload phase the specimen axial stress and the fluid pressure are kept equal (hydrostatic stress in the specimen) to avoid premature failure. When the desired confinement pressure is attained the test starts by increasing the axial load while leaving the fluid pressure constant. The nominal strain rate in this test is 0.001 s^{-1}. The axial strain of the specimen is measured during the test with a calibrated clip gage.

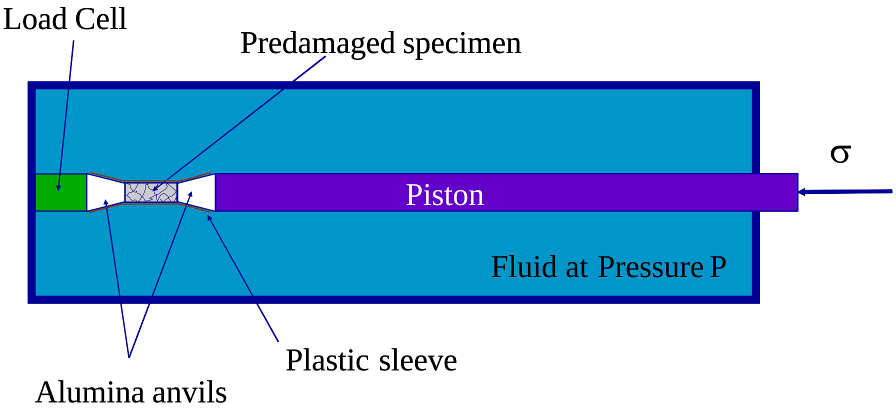
Load Cell
Predamaged specimen
σ
Piston
Fluid at Pressure P
Plastic sleeve
Alumina anvils

Figure 1. Hydraulic bomb experimental set-up.

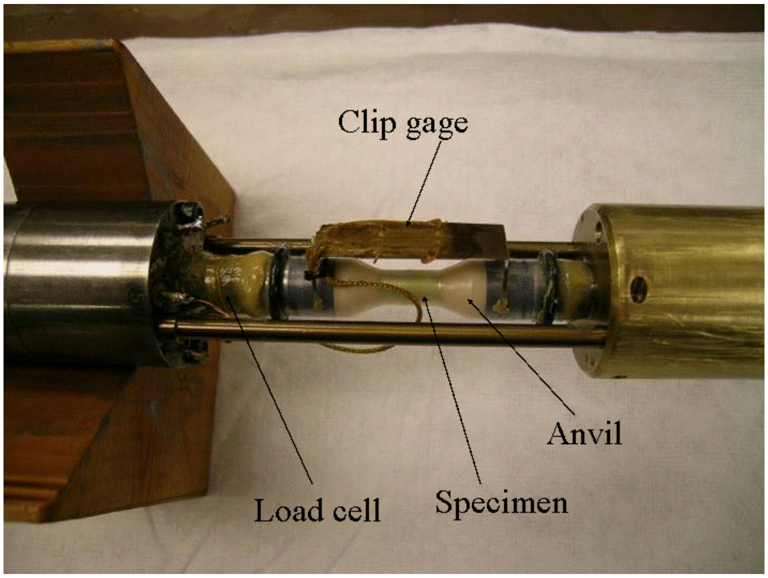
Clip gage
Anvil
Load cell
Specimen

Figure 2. Specimen placement before being inserted into the pressure vessel.

2.3 "Confined Sleeve" Technique

A second testing technique consists of placing the specimens inside a confinement sleeve. The experimental technique is described in Ref. [13] but is briefly presented here for completeness. The specimen is inserted into a Vascomax steel sleeve that is honed to fit the specimen. The sleeve outer diameter is 12.70 mm. An axial compressive stress is applied to the specimen with an MTS servohydraulic machine by means of two tungsten carbide (or SiC-N) platens.

The variables recorded during the test are the axial stress in the specimen measured by a load cell in the MTS machine; axial strain in the specimen, measured by a clip gage placed on the top and bottom platens; and axial and hoop strain in the sleeve, measured by a vertical and annular strain gages, respectively, on the sleeve. The hoop strain is used to infer the "internal pressure" of the sleeve, i.e., the radial stress that the specimen exerts on the sleeve, which is also the confinement pressure of the specimen. It is important to point out that the confinement pressure increases during the test. Acoustic emission was independently recorded to assist in determination of "events" that occur within the specimen during the test. The confined sleeve test is limited by the yield strength of the steel sleeve (the analysis for interpreting the data assumes that the sleeve remains elastic). Extensive discussion of interpretation and the results of this technique can be found in [12, 14-15].

The sleeve technique can also be applied to the split-Hopkinson bar. In this case, the sleeved specimen is placed between the incident and output bar of the split-Hopkinson bar. The steel confining sleeve, with the hoop strain gage in place, is shown in Fig. 3. Alumina and silicon carbide anvils are used to transfer the load from the bars to the specimen.

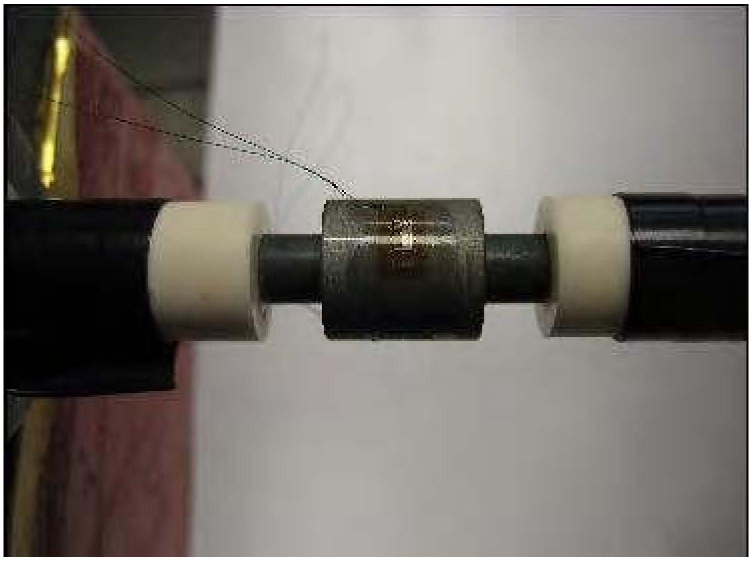

Figure 3. Confined sleeve test placed in the split-Hopkinson bar.

3.0 Results and Interpretation

3.1 Interpretation of the Hydraulic Bomb Experiments

The bomb tests are involved but their interpretation is, in principle, unambiguous. The axial stress is directly derived from the load measured with the load cell ($\tilde{\sigma}_z = \sigma_{eq} + \tilde{\sigma}_r$) and the hydrostatic pressure on the specimen is inferred from $P = (\tilde{\sigma}_z + 2\tilde{\sigma}_r)/3$.

The primary objective of this work is to evaluate how the failure stress of intact and damaged glass varies with pressure. As it will be discussed in Section 4, two well known constitutive models—the Drucker-Prager (DP) and Mohr-Coulomb (MC) models—can be used to interpret the data. For the DP model, the failure stress of the different specimens is plotted in a σ_{eq} versus P graph. For the MC model, following Desai's [2] recommendation, the failure points are plotted on a $(\sigma_1 - \sigma_3)/2$ versus $(\sigma_1 + \sigma_3)/2$ graph, where σ_1 and σ_3 are the maximum and minimum principal stress, respectively.

3.1.1 Intact Specimens

A total of twenty-two tests were performed on borosilicate glass in the pressure bomb. Six of the tests were on intact specimens; the other sixteen were performed on predamaged glass. The results of four typical tests are shown in Fig. 4. Tests BF-63 and BF-61 were performed on intact specimens at confinement pressures of 250 and 400 MPa, respectively. The dotted lines are straight reference lines that permit determination of when the measurements deviate from linearity. The exact cause of the nonlinearity is unknown (perhaps densification?), but this nonlinearity is not thought to be related to the propagation of cracks since failure for these specimens is "catastrophic." Failure occurs suddenly (denoted by the vertical arrows), and after failure, the load carrying stress is zero since the specimens "exploded" in compression.

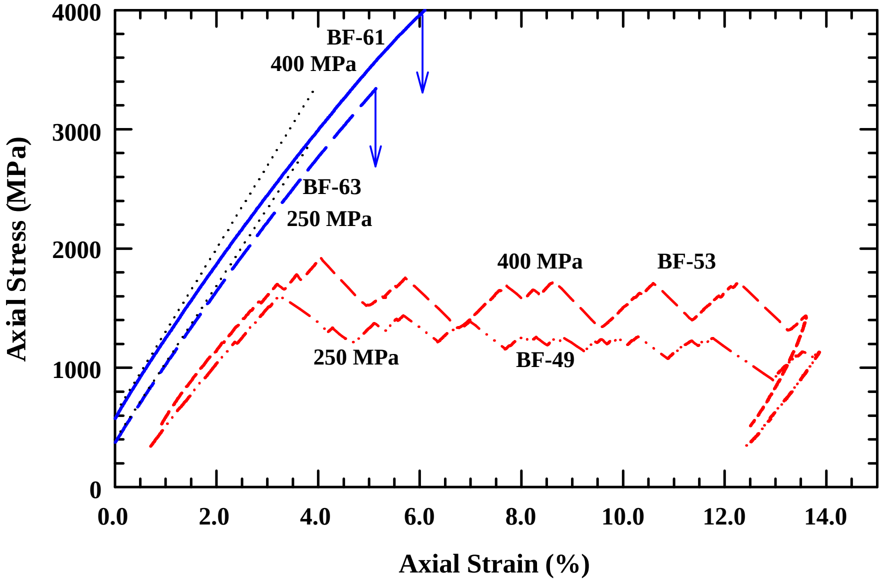

Figure 4. Two intact specimens (BF-61 and BF-63) and two predamaged specimens (BF-49 and BF-53) tested in the bomb at 250 and 400 MPa nominal confinement pressures.

3.1.2 Predamaged Specimens

Failure of predamaged specimens is very different, as shown in Fig. 4 for tests BF-49 and BF-53. Upon reaching some maximum axial stress, the load drops, but the specimen still supports a significant amount of load for large strains. The initial drop in load carrying capability (at 2-4% axial strain) results from the formation of a shear plane. The stress-strain curve after this initial failure has a sawtooth shape, probably because the failure surfaces of the shear plane slide over each other, occasionally "catching" and then releasing, creating the sawtooth pattern. The residual load is not a uniquely defined quantity; instead, the residual load is represented by the "peaks and valleys" of the sawtooth response.

3.2 Interpretation of the Confined Sleeve Experiments

3.2.1 Intact Specimens

A total of 9 intact specimens were tested in the sleeve. An example of a test with monotonic load of the specimen inside the steel sleeve is shown in Fig. 5. In this case there is no absolute maximum, but jumps or "failure avalanches" [16] occur. The maximum load attained in these tests was controlled by the operator, not the specimen strength. The jumps probably indicate the formation of a shear plane that is suddenly propagated. The planes slide against each other, but after a few microns of motion, propagation is stopped by the sleeve. Slip planes are apparent in the post-test analysis of the specimens as shown in Ref. [12]. The jumps are usually amplified on an axial stress versus hoop strain plot, Fig. 6. The hoop strain in the sleeve is very sensitive to specimen motion, so when failure occurs in the specimen and two planes slide, the jump in the hoop strain is large.

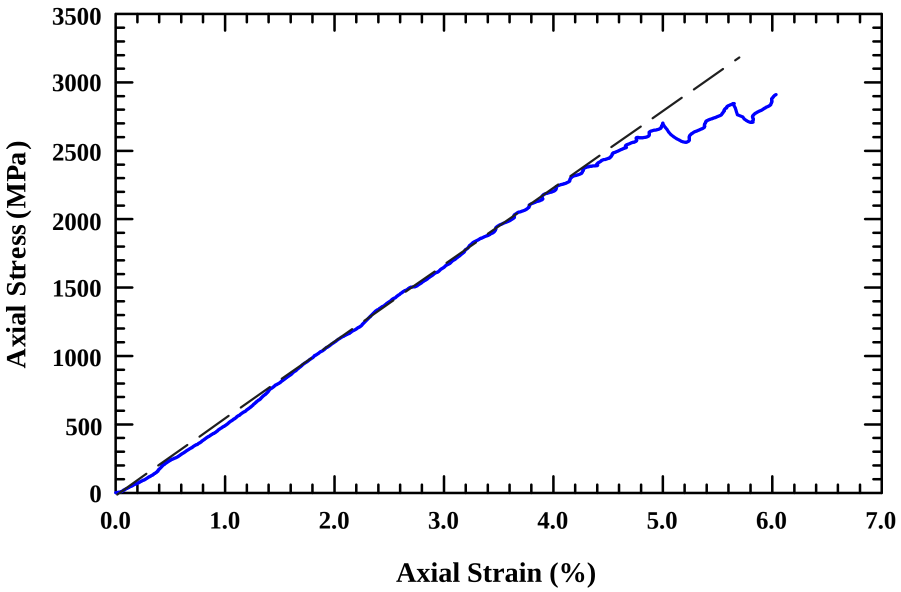

Figure 5. Stress vs. strain for an initially intact specimen in a confined sleeve test under monotonic load (test BF-17).

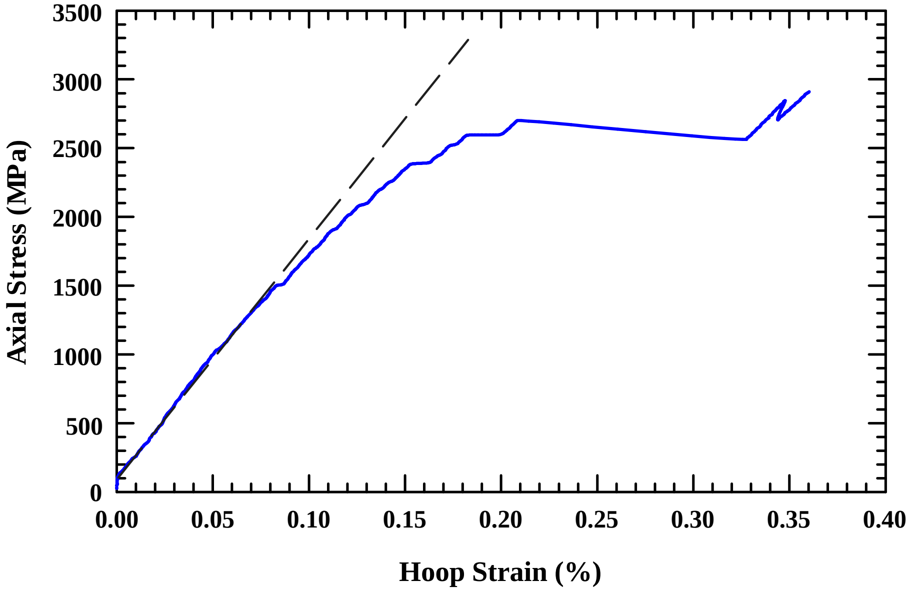

Figure 6. Stress vs. sleeve hoop strain for an initially intact specimen in a confined sleeve test under monotonic load (test BF-17).

3.2.2 Predamaged Specimens

Confined sleeve experiments were conducted on 18 predamaged specimens that were subjected to a maximum of 10 load cycles. An example is shown in Fig. 7, which plots the data in terms of equivalent stress versus hydrostatic pressure. The equivalent stress is again $\sigma_{eq} = \tilde{\sigma}_z - \tilde{\sigma}_r$ but now the confinement pressure $\tilde{\sigma}_r$ varies during the test. If the sleeve deforms elastically and uniformly, $\tilde{\sigma}_r$ can be calculated from the elastic solution (see for example Ref. [17]):

$$\tilde{\sigma}_r = \frac{E_{sl}}{2}\frac{b^2 - a^2}{a^2}\varepsilon_\theta \tag{2}$$

where E_{sl} is the elastic modulus of the sleeve, a and b are the internal and external radii, respectively, and ε_θ is the hoop strain of the sleeve. The elastic constants of the specimens can also be determined but a more elaborate model is needed; this was done for the predamaged specimens in Ref. [14] showing that if the material is well confined, a severely cracked specimen has elastic constants that are the same, within measurement uncertainties, as an intact specimen.

The interpretation of the jumps seen in Fig. 7 and how these jumps are “translated” to a constitutive model is shown in Fig. 8. A jump is a sudden discontinuity in the pressure applied to the specimen, probably due to the creation and slippage of an internal shear plane. The jumps occur while the applied axial load is increasing. It is thought that the jumps provide fundamental information of how the specimen fails at different confinement pressures. Consequently, all the jumps recorded in each of the tests (four jumps in the one shown in Fig. 8 for test BF-21) are placed on an equivalent stress versus pressure graph. The equivalent stress is computed from Eqn. (1) once the radial stress is calculated from the hoop strain gage. The right plot of Fig. 8 is a summary of the stress-pressure jumps recorded in all the experiments conducted on predamaged specimens in the confined-sleeve tests. In the example, there are four jumps in test

BF-21 (left figure) used to populate the right figure. It is noted that the hydrostatic pressure is a combination of the confining pressure and the pressure generated by the axial load.

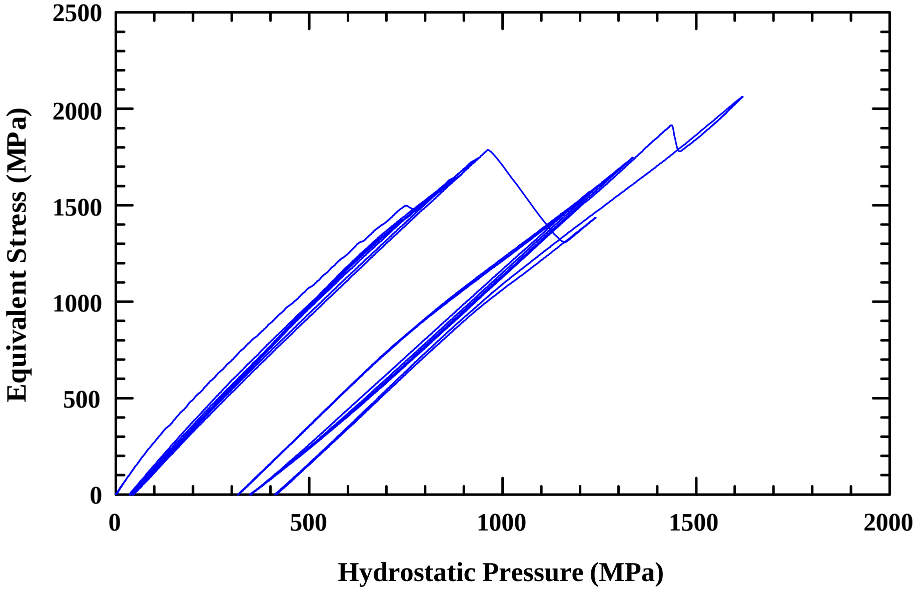

Figure 7. Equivalent stress vs. pressure for a predamaged specimen in a confined sleeve test under cyclic loading (test BF-14).

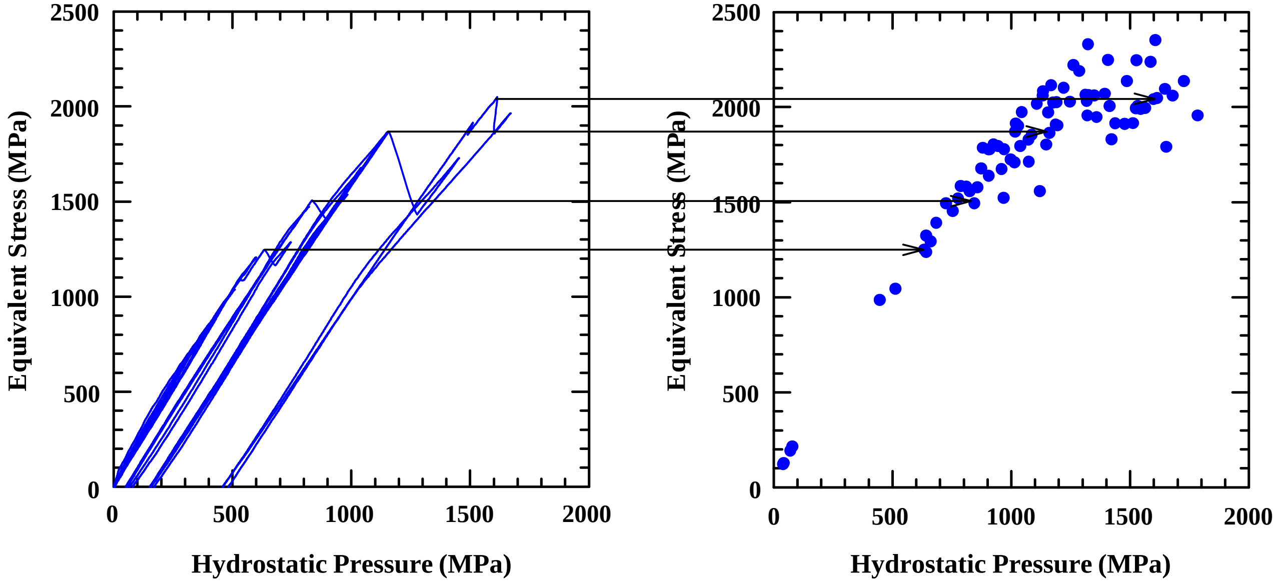

Figure 8. Interpretation of the sleeve tests with predamaged specimens.

4.0 Constitutive Model Parameters

4.1 Constitutive Models

Nonlinearities like the ones shown in Figs. 4 or 5—the deviation of data from the superimposed dashed and dotted lines—were ascribed to plasticity of the glass [14], although this may be due to nonlinear elasticity. It is known that some glasses or ceramics under confinement can flow plastically. For example, Peter [18] mentions that not all the flow phenomena in glasses can be explained as densification and argues that some glasses show properties compatible with classic plasticity. Other arguments for plastic flow can be found in Refs. [19-20].

In this work the approach will be a little different since the failure points will be assumed to define a flow surface. This approximation should be close to reality if the failure is not catastrophic; for example, when damaged specimens are tested in the bomb as in Fig. 4. So whenever the Drucker-Prager or Mohr-Coulomb models are mentioned below, it is understood that they represent failure surfaces that, when used in numerical simulations, will be used to limit the strength; however, we do not change the strength as a function of damage in the work reported here, as done by others, e.g., Holmquist and Johnson [21-22]. The data will be analyzed to determine constants for failure (a change in load-carrying capability) of intact glass and for damaged glass.

4.1.1 Drucker-Prager Model

The Drucker-Prager (DP) model [23] has the form:

$$Y = \begin{cases} Y_0 + \beta P & P < \left(Y_{cap} - Y_0\right)/\beta \\ Y_{cap} & P \geq \left(Y_{cap} - Y_0\right)/\beta \end{cases} \tag{3}$$

where Y_0 is the zero-pressure strength, β is the slope of Y versus P, P is the hydrostatic pressure (negative of the mean stress), and Y_{cap} is the limiting flow stress.

4.1.2 Mohr-Coulomb Model

Predamaged specimens tested in the bomb systematically showed a shear plane at an angle between 55 and 70 degrees. The angle seems to be independent of the applied confinement pressure. The DP model is based on the first invariant of the stress tensor, I_1, and the second invariant of the stress deviator tensor, J_2. The flow surface in the π-plane is a circle, and thus, the DP model can never have a characteristic failure angle. Incorporating the third invariant J_3 into the description of failure results in flow surface on the π-plane being a polygon, which then has a characteristic failure angle. The Mohr-Coulomb (MC) model incorporates J_3, and has a characteristic failure angle independent of the confinement pressure (see Ref. [24]); thus, it was felt that the MC model could be an appropriate candidate for describing the response of glass.

The data from the hydraulic bomb and confined sleeve tests were reanalyzed from the perspective of a MC model. Results for the predamaged bomb specimens are displayed in Fig. 4. The MC model gives the maximum shear stress, τ, that the glass can support on any plane:

$$\tau = c + \mu\tilde{\sigma}_n \tag{4}$$

where c is the cohesion, $\mu \equiv \tan(\phi)$ is the friction coefficient (ϕ is the friction angle), and $\tilde{\sigma}_n$ the normal stress (positive in compression).

4.2 Hydraulic Bomb Tests Results

4.2.1 Drucker-Prager Analysis

4.2.1.1 Intact Specimens

Failure data obtained from tests like the ones shown in Fig. 4 were plotted in an equivalent stress versus hydrostatic pressure graph, as shown in Fig. 9. The open triangles indicate intact unconfined tests, i.e., uniaxial stress tests, for which the load path is a straight line with a slope of three. All the confined tests (dark triangles) with the exception of BF-60 (shaded triangle) seem to be on a straight line with slope 1.2. Test BF-60 was the only non-catastrophic test with an intact specimen and, as such, is considered an outlier. We believe that the specimen failed during the preload making it, in fact, a predamaged specimen.

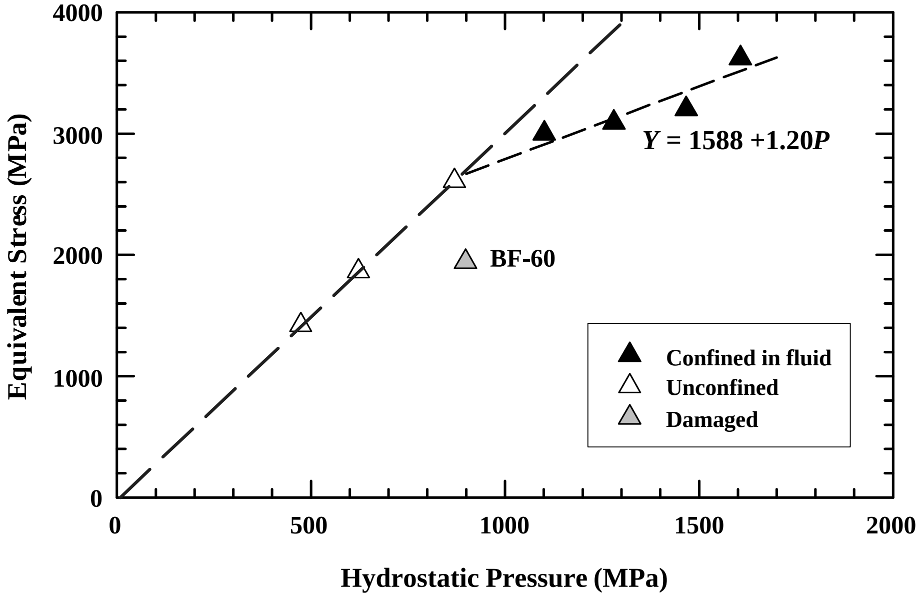

Figure 9. Equivalent stress at failure for different intact specimens tested in the hydraulic bomb.

For unconfined specimens the scatter in equivalent stress is very large, roughly from 1.4 GPa to 2.6 GPa. This scatter is inherent to brittle materials like glass; but, the scatter seems to decrease when the specimen is confined. The data in Fig. 9 suggests that an appropriate DP model for the intact specimens is:

$$\text{Confined Intact Strength:} \quad Y = 1.59 + 1.20P \quad (\text{GPa}) \tag{5}$$

4.2.1.2 Predamaged Specimens

Predamaged specimens have a very different behavior, since after failing the specimen is still able to carry load[2], as shown in Fig. 4. The peak load of the 16 tests performed is shown in Fig. 10. Three unconfined tests (open triangles) performed on predamaged specimens are also included in the plot. A linear regression fit performed through only the confined data provides the following DP model for predamaged specimens:

$$\text{Confined Predamaged Strength:} \quad Y = 0.423 + 1.22P \quad (\text{GPa}) \tag{6}$$

---

[2] Technically, the specimens that were initially intact and then fail could also carry a load, but failure is so catastrophic that the plastic sleeve is ripped apart and the comminuted specimen is dispersed in the hydraulic fluid.

The unconfined data were not included in the linear fit because the primary interest is on confined results. A very small confinement pressure, like the one used for test BF-57 (25 MPa), significantly increases the strength of the specimen from approximately 150 to 600 MPa.

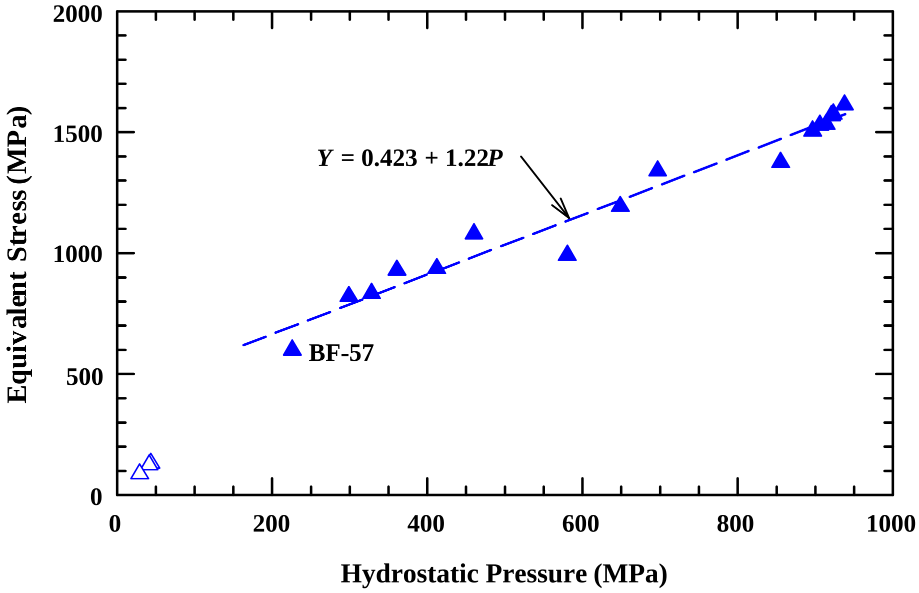

Figure 10. Equivalent stress at failure for different predamaged specimens tested in the bomb; unconfined tests are at the lower left.

The residual strength constants for the hydraulic bomb tests were obtained from the same tests that were used to estimate the predamaged constants, but using the sawtooth portions of the response. Analysis of the sawtooth portion of the curves of Fig. 4 is not straightforward since the specimen at this stage probably has a large amount of damage. It was decided to select three "characteristic" points along the curve, a local maximum, a local minimum, and an average. These points are plotted as σ_{eq} versus P in Fig. 11. The scatter is very large due to the oscillatory nature of the test results. The linear regression performed did not force the intercept in the (0,0) point although it would be reasonable to think that at zero pressure these specimens have very small strength.

$$\text{Confined Residual Strength: } Y = 0.14 + 1.3P \quad \text{(GPa)} \tag{7}$$

It is remarkable that the slopes for the intact, predamaged and residual strength are very similar (1.2 to 1.3). This might be just a coincidence but it simplifies modeling the damaged glass since damage seems to be affecting principally the strength at zero pressure and not the slope.

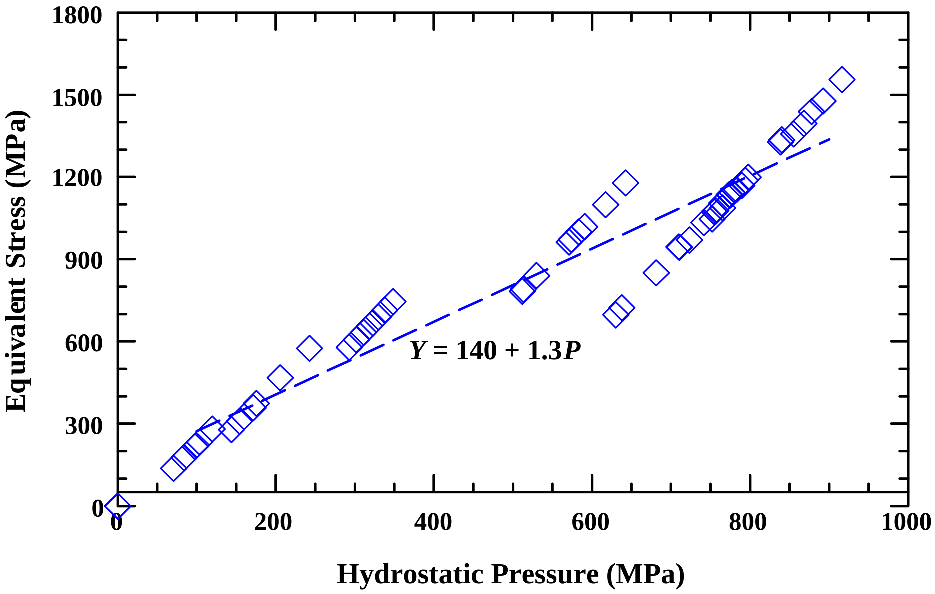

Figure 11. Residual equivalent stress for specimens tested in the hydraulic bomb.

4.2.2 Mohr-Coulomb Analysis

Predamaged specimens tested in the bomb systematically showed a shear plane at an angle between 55 and 70 degrees. The angle seemed to be independent of the confinement pressure applied to the specimen, see Fig. 12. When performing numerical simulations of the bomb test it was realized that a DP model can never have a characteristic failure angle since the DP model is based only on I_1 and J_2, the first and second invariants of the stress deviator tensor. A characteristic angle can arise only if the flow surface on the π-plane is not a circle but a polygon, i.e., the third invariant J_3 enters in the flow surface equation. The Mohr-Coulomb model includes J_3, and a characteristic failure angle independent of the confinement pressure arises naturally from the model (see Ref. [24]). The flow surface will be discussed in detail in Section 6.2.2.

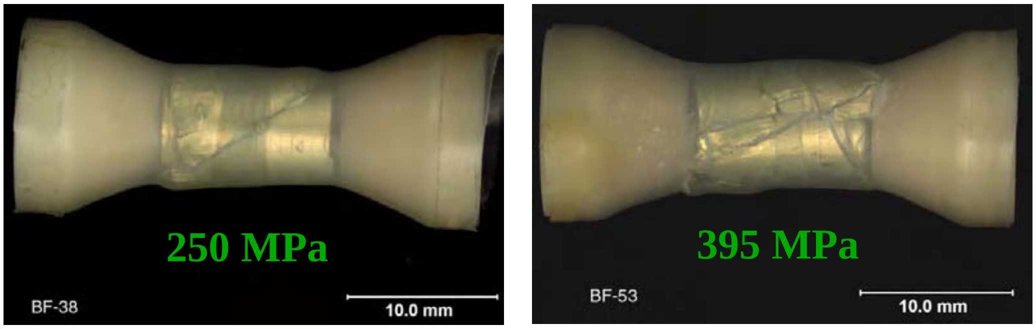

Figure 12. Two predamaged specimens that were tested in the bomb at 250 and 400 MPa confinement pressure. Shear angles were very similar for the whole range of confinement pressures, from 25 to 400 MPa.

4.2.2.1 Intact Specimens

The same intact data shown on Fig. 9 are now analyzed and plotted from a MC perspective in Fig. 13. The MC model gives the maximum shear stress τ a solid can support on any plane, Eqn. (4). A linear least squares regression[3] in the $(\sigma_1 - \sigma_3)/2$ versus $(\sigma_1 + \sigma_3)/2$ representation was performed to the test data to obtain an intercept of a = 651 MPa and the slope b = 0.506. The relation between these curve-fit constants and MC parameters, Eqn. (4), is given by:

$$\phi = \arcsin(b) \qquad \mu = \tan(\phi) \qquad c = a/\cos(\phi) \tag{8}$$

so for the intact specimens a MC model can be written as:

$$\text{Confined Intact Strength: } \tau = 0.755 + 0.587\,\tilde{\sigma}_n \quad \text{(GPa)} \tag{9}$$

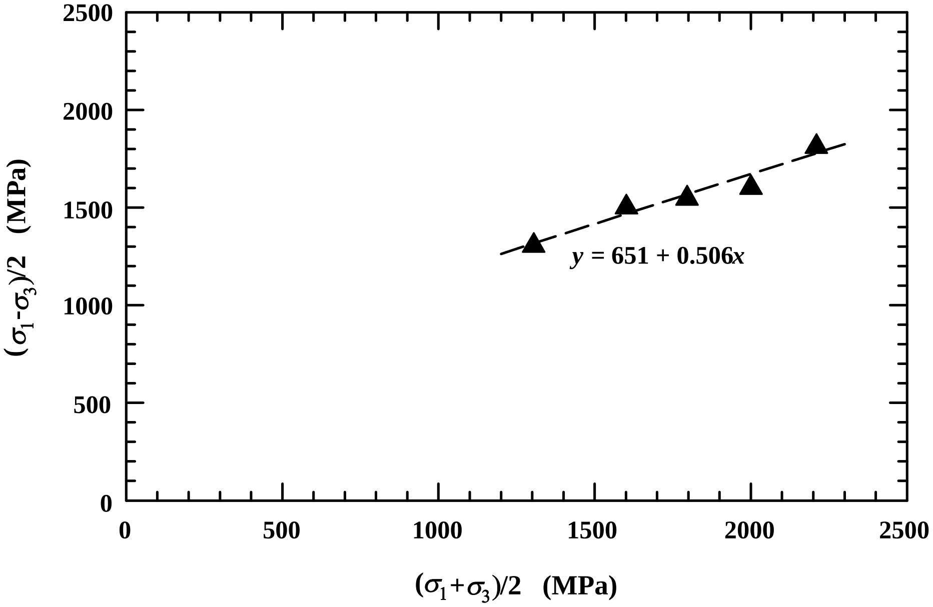

Figure 13. MC failure points for intact specimens tested in the bomb. σ_1 and σ_3 are the maximum and minimum principal stresses respectively.

4.2.2.2 Predamaged Specimens

As discussed in reference to Fig. 4, the predamaged specimens do not fail catastrophically like the intact specimens. After the first peak, the specimens were still able to carry a load that oscillated, in a sawtooth manner, around a value ~10% less than the first peak. The maximum or peak load is considered the “strength” of the predamaged specimen and is plotted in Fig. 14. These data happen to align very nicely since a linear fit gives a regression coefficient of 0.94. The slope is the same as the intact slope, b = 0.51, but the value at the origin is much lower, i.e., $a = 173$ MPa instead of 651 MPa. For the MC constitutive model for predamaged specimens, this implies:

$$\text{Confined Predamaged Strength: } \tau = 0.201 + 0.594\,\tilde{\sigma}_n \quad \text{(GPa)} \tag{10}$$

---

[3] Regression fits are done in the form of $y = a + bx$.

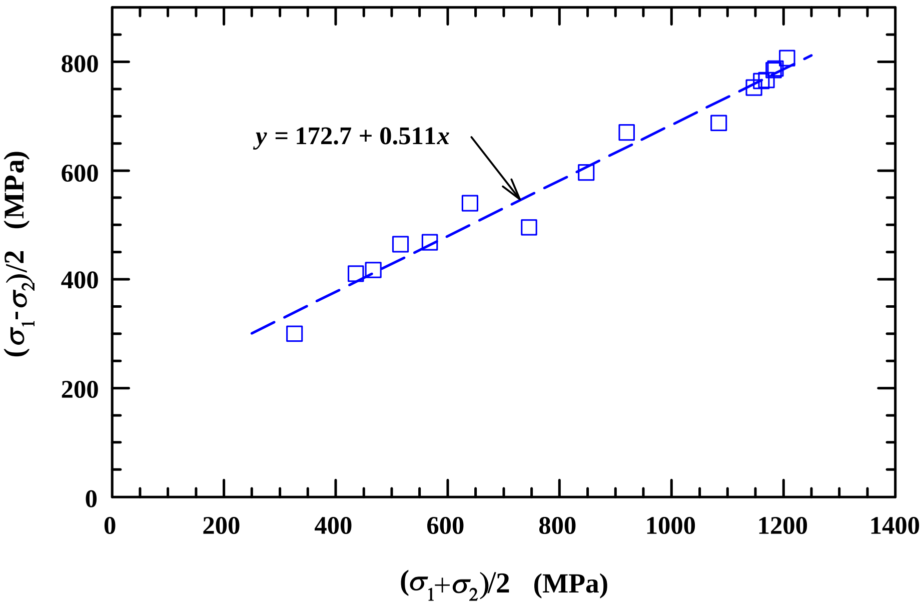

Figure 14. MC failure points for the damaged specimens tested in the bomb.

As in the DP analysis, the sawtooth portion of the response was also analyzed. Again three "characteristic" points were used to select a maximum, a minimum, and an "average" point along the sawtooth curve. The result is shown in Fig. 15.

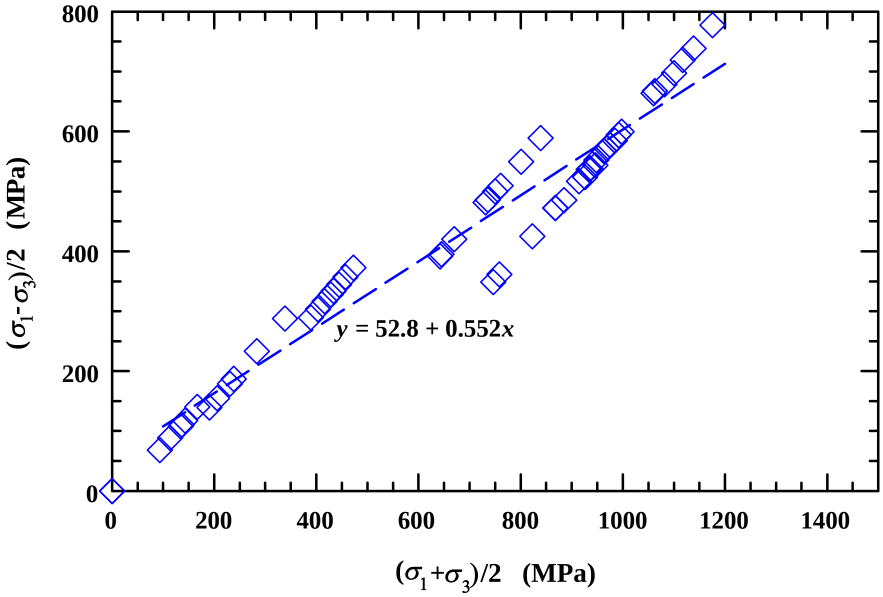

Figure 15. MC residual strength data for predamaged specimens tested in the bomb.

The scatter is large for the residual strength data. A linear fit to the data should be used with care owing to the nature of the data. A MC constitutive model for residual ("heavily damaged") glass could be:

$$\text{Confined Residual Strength: } \tau = 0.063 + 0.66\,\tilde{\sigma}_n \quad \text{(GPa)} \qquad (11)$$

It is clearly reasonable to assume that damage in the intact specimens is less than damage in the predamaged specimens. Also the residual strength measured in the bomb corresponds to a specimen with more damage than a predamaged specimen. As with the DP analysis, it is remarkable (maybe only a coincidence) to see that the friction coefficients for the intact, predamaged, and residual glass are very similar, ~0.6, while the cohesion is severely diminished with increasing levels of damage. Actually this fact could simplify a damage model in that *damage seems only to affect cohesion of the glass.*

4.3 Confined Sleeve Tests Results

Sleeve test results were presented in Chocron, *et al*. [15]. However; since more experimental data are now available, resulting in a refinement of the previous analyses, the data will be briefly revisited.

4.3.1 Drucker-Prager Analysis

As described in Section 4.2, all the jumps recorded in the confined sleeve tests were transferred to an equivalent stress versus pressure plot. Results for intact and predamaged specimens confined in the sleeve are shown in Fig. 16. The unconfined specimens are also included in the graph. The scatter in these tests is much larger than in the hydraulic bomb, so the linear fits through the data have smaller correlation coefficients.

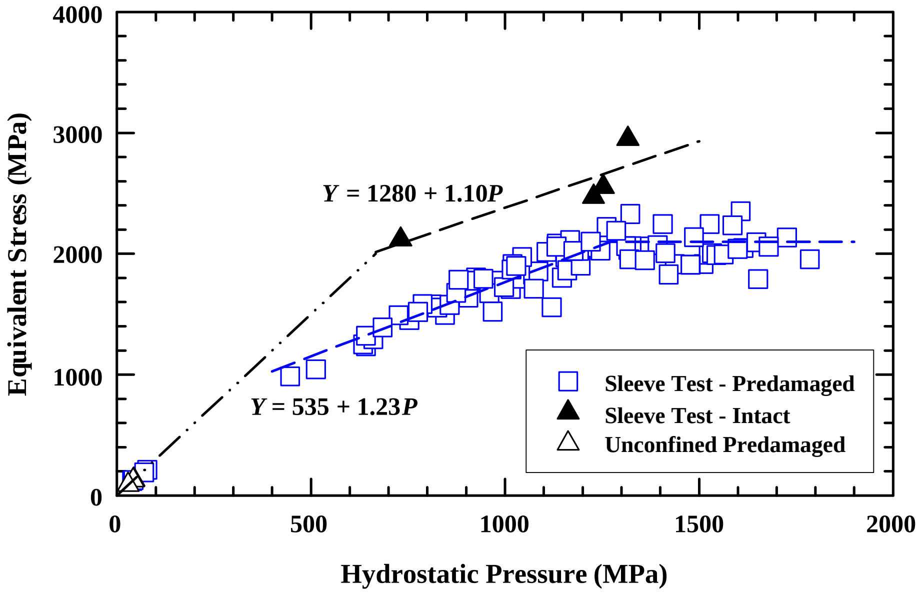

Figure 16. DP constitutive models inferred for intact and predamaged specimens.

In fact, the intact data should be used with care since testing intact specimens inside the sleeve was very challenging. It is thought that even though the sleeve was honed to fit the specimens, any misalignment or eccentricity affects the results of the intact specimens significantly. For the intact specimens the DP equation obtained is:

$$\text{Confined Intact Strength:}\quad Y = 1.28 + 1.10P \quad (\text{GPa}) \qquad (12)$$

For the predamaged specimens the DP equation obtained is:

$$\text{Confined Predamaged Strength:}\quad Y = 0.535 + 1.23P \quad (\text{GPa}) \qquad (13)$$

It is also observed that, for the predamaged material, that the strength (equivalent stress) appears to have reached a plateau at a pressure of approximately 1.3 GPa, after which the strength is independent of the pressure, i.e., a cap. There is scatter in the data, but this cap has a value of about 2.1 ± 0.2 GPa. This will be discussed in more detail in Sections 6 and 7.

4.3.2 Mohr-Coulomb Analysis

Figure 17 shows the same data presented in the previous section but analyzed from the MC perspective.

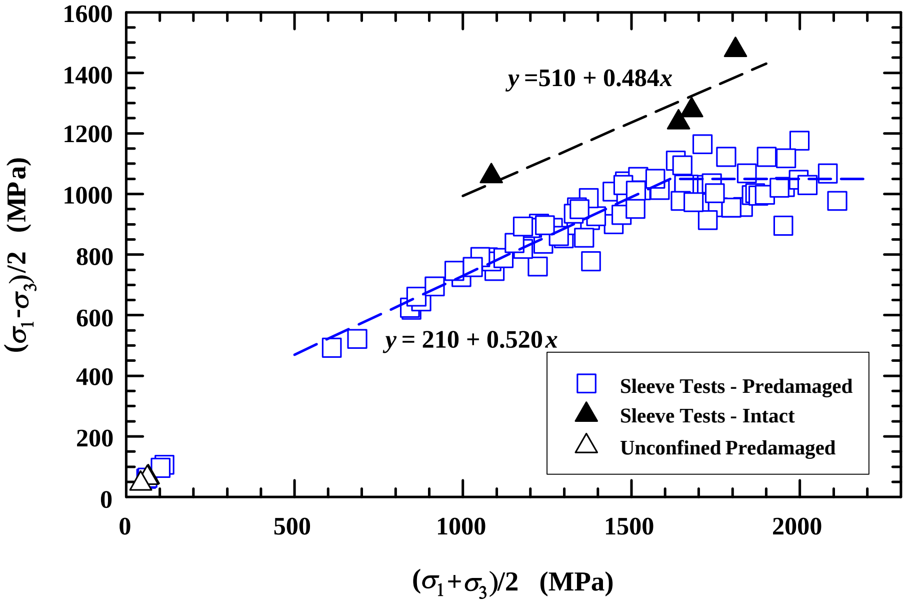

Figure 17. MC constitutive models inferred for intact and predamaged specimens.

The equations obtained, using the same method as the one presented in Section 4.2.2, for the intact specimens is:

$$\text{Confined Intact Strength: } \tau = 0.583 + 0.553\tilde{\sigma}_n \quad \text{(GPa)} \tag{14}$$

And for the predamaged specimens:

$$\text{Confined Predamaged Strength: } \tau = 0.246 + 0.609\,\tilde{\sigma}_n \quad \text{(GPa)} \tag{15}$$

The shear stress appears to achieve a maximum value (a cap) in Fig. 17 (similar to Fig. 16). Therefore, Eqn. (15) is applicable up to a maximum normal stress of approximately 1.3 GPa—or ½(σ_1 + σ_2) = 1.65 GPa—and then reaches a plateau with a value of approximately 1.05 GPa.

4.4 Summary of Constitutive Model Results

The constitutive parameters for the Drucker-Prager model and the Mohr-Coulomb model are summarized for intact, predamaged, and residual strength borosilicate glass in Tables 2 and 3, respectively. A few observations can be made. First, the parameters were determined by least-squares regression fits to the experimental data. Although three significant figures are given for the various parameters, the parameters should only be considered to be accurate to—at best—two significant figures. Additionally, as is evident from Figs. 11 and 15, the parameters for the residual strength should be considered as average values that are representative of highly damaged material.

It is quite satisfying that the two experimental methods (the bomb tests and the confined sleeve tests) yield comparable values for the constitutive parameters. This provides confidence in the results of the confined sleeve experimental procedures and interpretation. Additionally, and as already pointed out, it is rather remarkable that β for the Drucker-Prager model and μ for the Mohr-Coulomb model seem to be relatively independent of the damage, whereas Y_0 and c decrease with increasing damage.

Table 2. DP Parameters for Intact and Predamaged Borosilicate Glass ($Y = Y_0 + \beta P$)

	Bomb Tests		**Sleeve Tests**	
Specimen	**Y_0 (GPa)**	**β**	**Y_0 (GPa)**	**β**
Intact	1.59	1.20	1.28	1.10
Predamaged	0.423	1.22	0.535	1.23
Residual	0.140	1.3	–	–

Table 3. MC Parameters for Intact and Predamaged Specimens ($\tau = c + \mu\,\tilde{\sigma}_n$)

	Bomb Tests		**Sleeve Tests**	
Specimen	**c (GPa)**	**μ**	**c (GPa)**	**μ**
Intact	0.755	0.587	0.583	0.553
Predamaged	0.201	0.594	0.246	0.609
Residual	0.063	0.66	–	–

5.0 Numerical Simulations of Characterization Tests

5.1 Introduction

The ultimate objective of the project is to understand the behavior of glass and to be able to simulate penetration phenomena. Numerical simulations require constitutive models and material constants for the materials typically in the form of an equation of state and a plasticity model. For strong, brittle materials, constitutive constants have typically been determined from both material characterization tests in the laboratory and ballistic tests, see for example Holmquist [21-22]. The ballistic tests are used to back-out constants that are difficult to measure under controlled laboratory conditions.

In the preceding sections, constitutive constants have been determined for two pressure-dependent constitutive models using laboratory characterization experiments. We now examine how well using these constants in numerical simulations can reproduce the characterization experiments (Section 5) and ballistic experiments (Section 6). In this section, the confined sleeve and hydraulic bomb tests were reproduced numerically. Replication of the experimental results by simulations does not validate the constitutive constants; but agreement shows self-consistency. Validation requires application of the models (and constants) to *independent* experiments and showing agreement between simulation results and the experiment. In Section 6, the Drucker-Prager (DP) and Mohr-Coulomb (MC) models are used in numerical simulations of ballistic experiments of a long gold rod into borosilicate glass; the numerical results are compared to the results of the experiments.

5.2 LS-DYNA Simulations of the Characterization Tests

5.2.1 Hydraulic Bomb Tests

The bomb tests with predamaged specimens were simulated using LS-DYNA. The 3-D cylindrical mesh was generated with True-Grid. Fourteen elements were used across the radius. The fluid pressure was simulated as a pressure boundary condition on the specimen. Both Drucker-Prager and Mohr-Coulomb plasticity models were investigated. The constants used were the ones obtained from the laboratory tests (Tables 2 and 3). Both models were able to give correctly the axial stress versus axial strain response but the DP model was not able to match the systematic failure pattern observed in the tests. This should be no surprise since the flow surface in the DP model is a circle, which does not have any characteristic or preferred failure angle.

On the other hand, the MC model has an unambiguous failure angle that can easily be determined analytically: $\theta_f = \pi/4 - \phi/2$, where θ_f is the failure angle and ϕ is the angle of friction of the specimen. Table 4 lists the parameters used in the simulations, where E, ρ, ν, μ, c are, respectively, the elastic modulus, density, Poisson's ratio, friction coefficient, and cohesion. These parameters differ slightly from the ones presented in Tables 1 and 4 because the ones used here were estimated relatively early in the test program. The small differences do not change the main conclusions. According to the parameters used in the simulations, the failure angle should then be $\theta_f = \pi/4 - \tan^{-1}(\mu)/2 = 30.4°$; and the complementary angle is 59.6°. These angles are in good agreement with the failure angles measured in the experiments (55°-70°), as shown in Fig. 18.

Table 4. MC Parameters Used in LS-DYNA Simulations for Predamaged Specimens

E (GPa)	ρ (g/cm^3)	ν	μ	c (GPa)
59	2.2	0.19	0.56	0.219

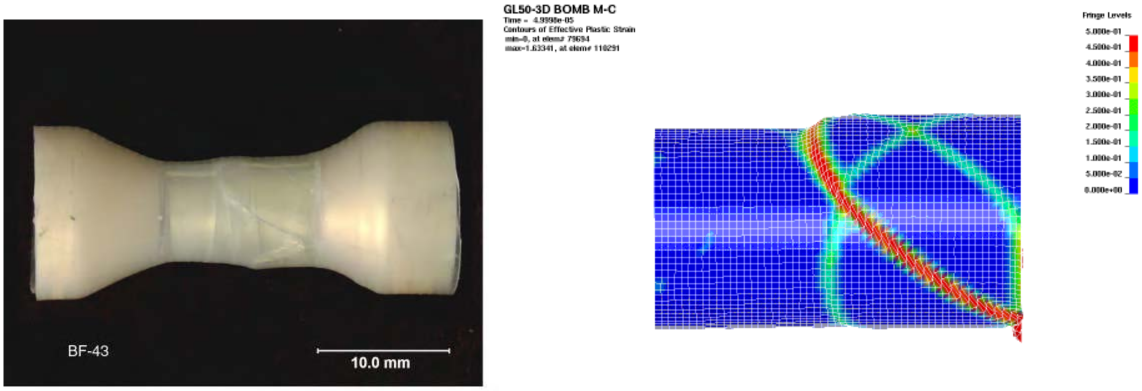
BF-43
10.0 mm
GL50-3D BOMB M-C
Time = 4.9998e-05
Contours of Effective Plastic Strain
min=0, at elem# 79694
max=1.63341, at elem# 110291
Fringe Levels
5.000e-01
4.500e-01
4.000e-01
3.500e-01
3.000e-01
2.500e-01
2.000e-01
1.500e-01
1.000e-01
5.000e-02
0.000e+00

Figure 18. The failure of a predamaged specimen tested in the bomb at 400 MPa radial confining pressure is compared to specimen simulated with DYNA.

Figure 19 shows that the MC model can reproduce quite well the stress-strain curves. LS-DYNA simulations at different confinement pressures are compared directly to experimental results to verify that the failure point is properly predicted. The oscillations of load (sawtooth patterns) are not captured by the model, probably because they are a consequence of the roughness (catching and releasing) of the failure surface created, something this numerical model would not be able to reproduce. But overall, given the scatter inherent in failure, the simulations reasonably replicate the experiments.

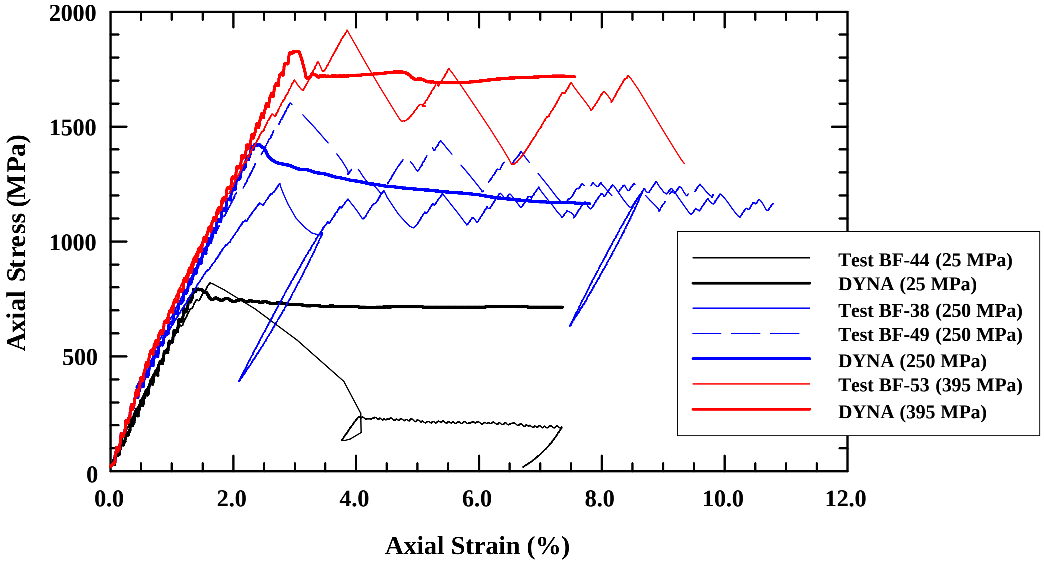

Figure 19. Stress strain curves computed with LS-DYNA using the MC model are compared to test data.

5.2.2 Sleeve Tests – Static

The quasistatic sleeve tests were also simulated in LS-DYNA. Both the DP and MC models were used for the damaged glass. Early in the program the DP model was used to check that the sleeve tests were being properly interpreted, as discussed in Dannemann, *et al.* [25]. It became apparent that the DP model was unable to reproduce the failure pattern (as already discussed) seen on the sleeve specimens, see Fig. 20, left. The image shows a predamaged specimen after being tested under sleeve confinement. Shear planes are apparent. The most prominent shear plane forms a 63° angle, very close to the angles observed in the bomb experiments.

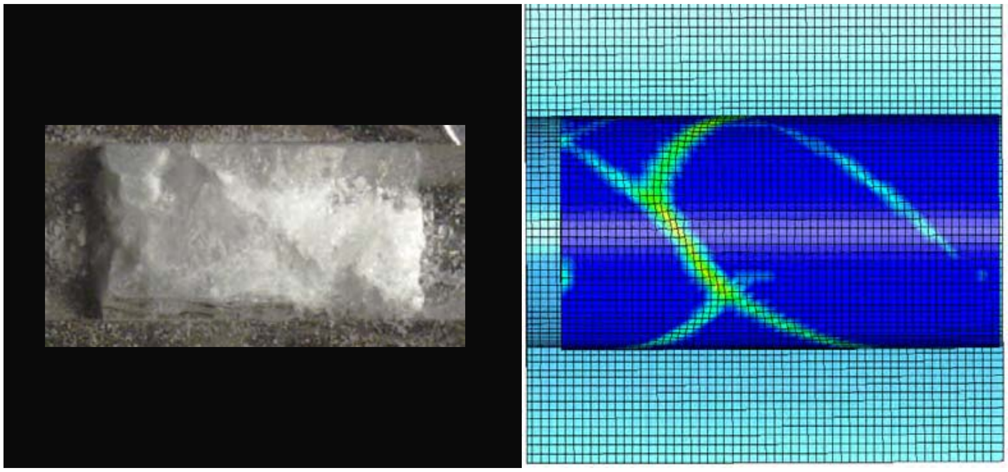

Figure 20. Test BF-14. Failure pattern for a predamaged specimen tested in the sleeve (left). Failure pattern obtained with the MC model in LS-DYNA (right).

The MC model, using the parameters in Table 4, was used to simulate the quasistatic sleeve tests. A prescribed displacement was applied to the numerical specimen (the left end in Fig. 20b). Also, the right end of the specimen, and the end of the sleeve, had their axial motion locked. Figure 20b shows the sleeve and mesh used in the simulations. Failure patterns were satisfactorily reproduced (a failure angle of 60°, as shown in Fig. 20, right.

5.2.3 Sleeve Tests – Dynamic

A numerical model of the full 3-D Hopkinson Bar was implemented in LS-DYNA to simulate a predamaged specimen being tested in the sleeve. Since the dynamic properties of the glass were unknown, the static material model was used as presented in Table 4. Figure 21 shows the details of a section around the specimen. No planes of symmetry were used in the simulation.

The specimen had 14 elements through the diameter, so the elements were approximately cubes with 0.0453 cm per side. The elements on the input and output bar were not cubes but elongated prisms. Their length was 1.24 cm. Figure 22 compares the input signal obtained in two tests with the signal of the numerical simulation. The numerical signal overshoots slightly probably due to the shape of the elements. The reflected signal is also slightly delayed probably because of small differences of the position of strain gages between the simulation and experiment. These differences were not considered a major concern.

The output signal for the two tests and the numerical simulation are compared in Fig. 23. The output signal is proportional to the axial stress being felt by the specimen. As seen in the figure, the numerical simulations, other than small differences, successfully reproduce the stress experienced by the specimens.

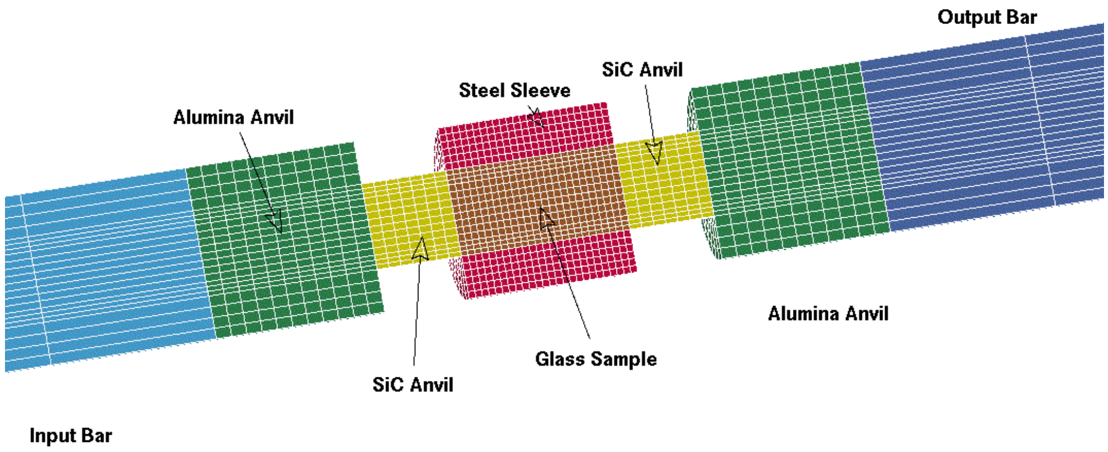

Figure 21. Mesh and materials for the LS-DYNA model of the split-Hopkinson bar.

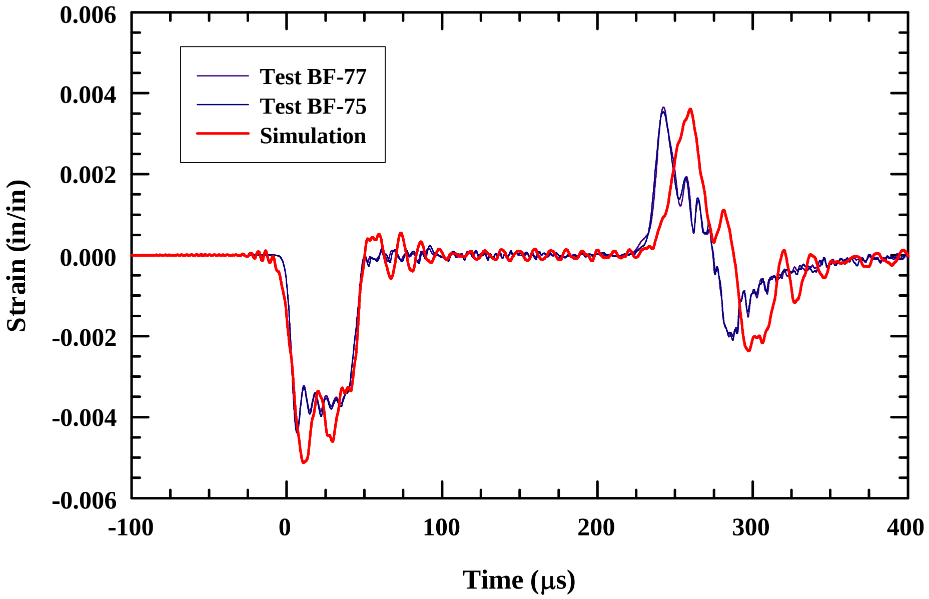

Figure 22. Signal recorded by a strain gage placed on the input bar for two experiments (BF-75 and BF-77) and for the numerical simulation.

Simulations of the hoop-strain signal (measured on the confining sleeve) are compared to experiment in Fig. 24. In this case the numerical simulation signal is “noisy” (perhaps because of hour-glassing of the elements) but lies on top of the experimental results, i.e., the simulations capture very well the hoop strain versus time response.

Finally Fig. 25 shows the equivalent stress versus pressure curves for the two tests and two numerical simulations, one that used a DP model and one with the MC model. The strain rate for the tests and simulations is estimated to be ~1500 s^{-1}. Since the numerical simulations reproduce the experimental results using a quasistatic constitutive model, it is concluded that any *strain rate effect is not significant for borosilicate glass* at these strain rates. That the strength is not strain-rate dependent under confinement has also been confirmed by others [7].

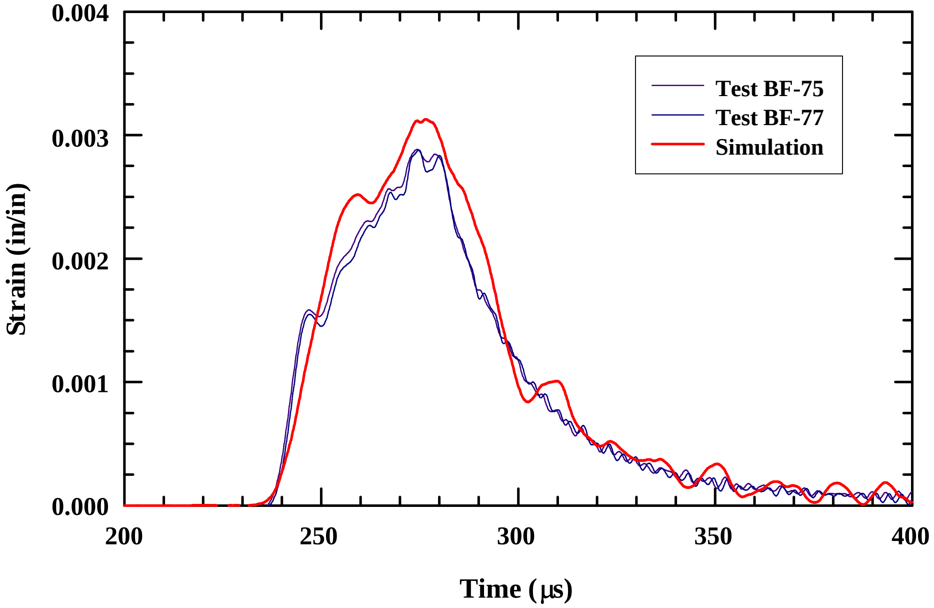

Figure 23. Signal recorded by a strain gage placed on the output bar for two experiments (BF-75 and BF-77) and for the numerical simulation.

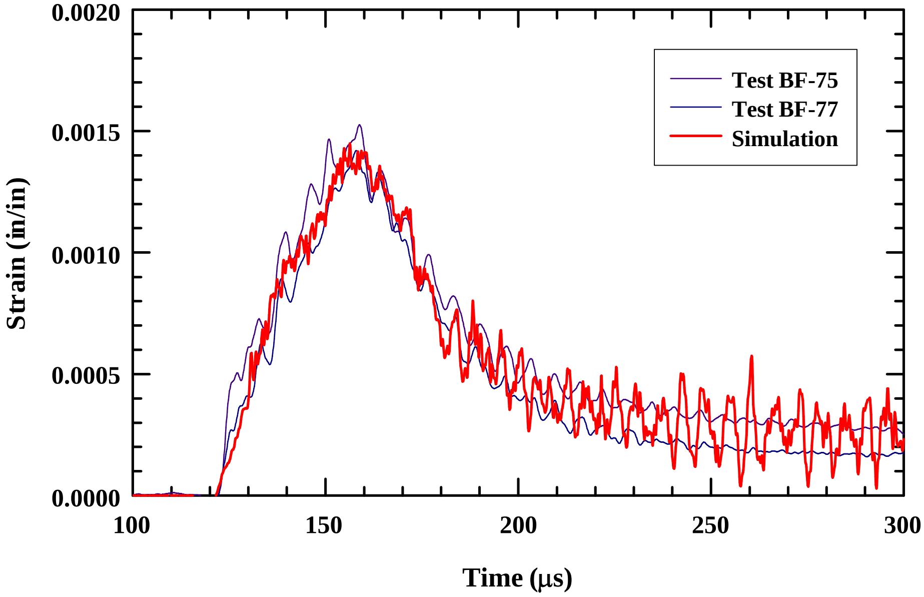

Figure 24. Signal recorded by a strain gage placed on the sleeve for two experiments (BF-75 and BF-77) and for the numerical simulation.

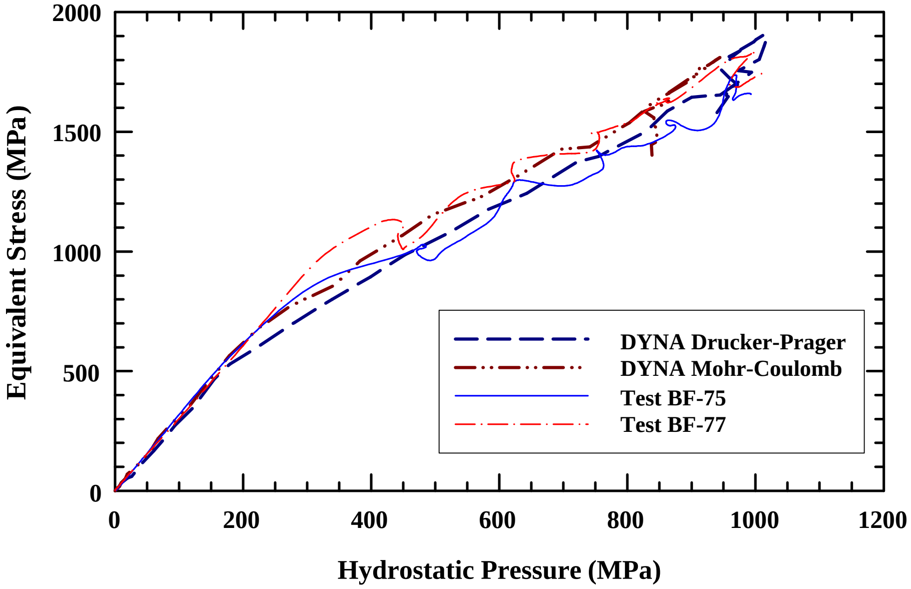

Figure 25. Signal recorded by a strain gage placed on the confining sleeve for two experiments (BF-75 and BF-77) and for the numerical simulation.

6.0 Numerical Simulations of Reverse Ballistic Experiments

6.1 Introduction

We now apply the two constitutive descriptions to the penetration of glass. Behner, *et al.* [1], performed long-rod penetration experiments of gold (Au) rods into intact Borofloat®33 glass cylinders with a length of 60 mm and a diameter of 20 mm. The pure Au rods had a diameter of 1 mm and a length of 50 or 70 mm. The experiments were conducted in the reverse ballistics mode where the glass target was launched at the suspended Au rod, which was aligned using a laser. The impact velocity (v_p) was varied over a range of approximately 0.4 to 3.0 km/s. Flash radiographs were used to obtain penetration-time and rod length-time data. The slopes of the linear regression fits to the data provide the penetration (u) and consumption velocities (v_c), respectively, which are plotted in Fig. 26 as a function of v_p. High-speed photography was also used to measure the propagation of the failure front in the glass. More details of the experiments are given in Ref. [1].

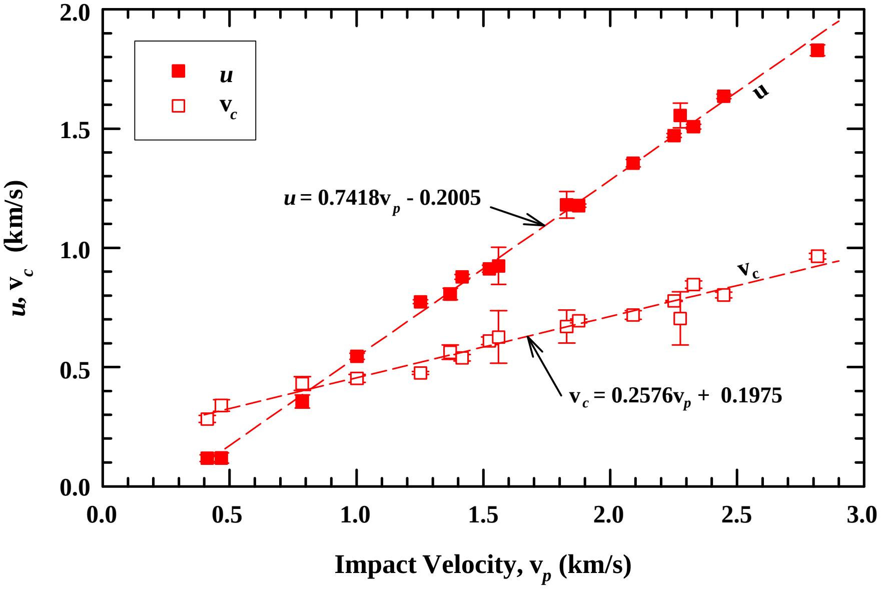

Figure 26. Penetration and consumption velocities vs. impact velocity for borosilicate glass impacted by gold rods (regression lines recalculated to include highest velocity data points).

It is assumed that the Au rod projectile penetrates failed glass [1]. This is not exactly true at the very beginning of penetration, and details of the transition of intact to failed glass might be important at early times. However, for the range of impact velocities studied here, the failure front propagates at least twice as fast as the rod is penetrating; thus, it would appear that the assumption that the rod penetrates failed material is reasonable. We thus avoid needing a description of how the glass fails. The results of the laboratory experiments are now used to determine constitutive constants for computational material models to describe the strength of failed glass as a function of confinement pressure.

The nonlinear wave propagation and material response computer program CTH [26] was used to conduct the numerical simulations. CTH contains a wide range of equations of state and viscoplastic models. Although the DP model was resident within CTH, the MC model was not; thus, the MC model needed to be implemented (as described in the Section 6.2). In addition to the inelastic response of the glass, as represented by either the DP or MC models, the elastic behavior of the damaged material must be modeled. It has been shown that if the material is well confined, a severely cracked specimen has elastic constants nearly the same as an intact specimen [15]; thus, the elastic response of failed material is taken as same as that of the intact material.

The Mie-Grüneisen equation of state was used to describe the thermodynamic response of the glass and the Au rod. The bulk modulus is 33.23 GPa; it was assumed that the glass had no nonlinear compressibility effects, i.e., $P = \kappa(\rho/\rho_o - 1)$, where κ is the bulk modulus, and the subscript "*o*" refers to the initial density. This is clearly an oversimplification, but it is believed that the penetration velocity would only be marginally affected by the inclusion of nonlinear terms. However, this assumption will be explored in future simulations. The Grüneisen coefficient (Γ) was set to 1.0. The Steinberg-Guinan model was used to describe the equation of state and constitutive response of the Au [27], which has a density of 19.3 g/cm^3. Seven zones were used to resolve the radius of the projectile (cylindrical symmetry), and this zoning was used throughout the problem.

6.2 Implementation of the Mohr-Coulomb Model in CTH

6.2.1 Introduction

CTH is a nonlinear wave propagation and material response (hydrocode) computer program developed by Sandia National Laboratories [26]. CTH contains a wide range of equations of state and viscoplastic models that can be selected by the user, depending upon the problem. For brittle materials like ceramics or glass, which have a strength that is pressure dependent, the typical choices would be the Johnson-Holmquist [23] or Drucker-Prager models. As mentioned earlier, although the DP model can successfully reproduce stress-strain curves obtained in the pressure bomb, it lacks the capability of reproducing a failure pattern like the one observed in the experiments. Since it was not known how important this feature would be when simulating projectile penetration, it was decided to implement the MC model into CTH.

6.2.2 Flow Surface and Implementation

Nayak [28] developed an equation for the MC flow surface that can be very conveniently implemented in hydrocodes:

$$F = \sigma_m \sin\phi + \bar{\sigma}\cos\theta_0 - \frac{\bar{\sigma}}{\sqrt{3}}\sin\theta_0 \sin\phi - c\cos\phi = 0 \tag{16}$$

where $\sigma_m = \sigma_{ii}/3$ is the mean stress, $\bar{\sigma}$ is the equivalent stress, and θ_0 is the Lode angle defined by:

$$\theta_0 = \frac{1}{3}\arcsin\left(-\frac{3\sqrt{2}}{2}\frac{J_3}{\bar{\sigma}^3}\right) \tag{17}$$

J_3 is the third invariant of the stress deviator tensor. CTH uses radial return for most of its viscoplastic models, for example, the von Mises and Drucker-Prager models. That means that the flow rule is non-associative but the return is done in the π-plane and at constant pressure. To circumvent the implementation of the radial return and stress rotations, CTH was modified to use, where possible, algorithms already in CTH. The subroutine implemented calculates *F* according to Eqn. (16) for each cell and time step. The algorithm first assumes that the response is completely elastic. If $F \leq 0$, nothing more needs to be done; but, if $F > 0$, the cell material is yielding and the subroutine computes the radial return scaling factor to bring the deviatoric stress back to MC surface, see Fig. 27. It also computes the strength as if it were a von Mises flow surface. This strength is then passed on to CTH so CTH can actually perform the radial return and stress rotations.

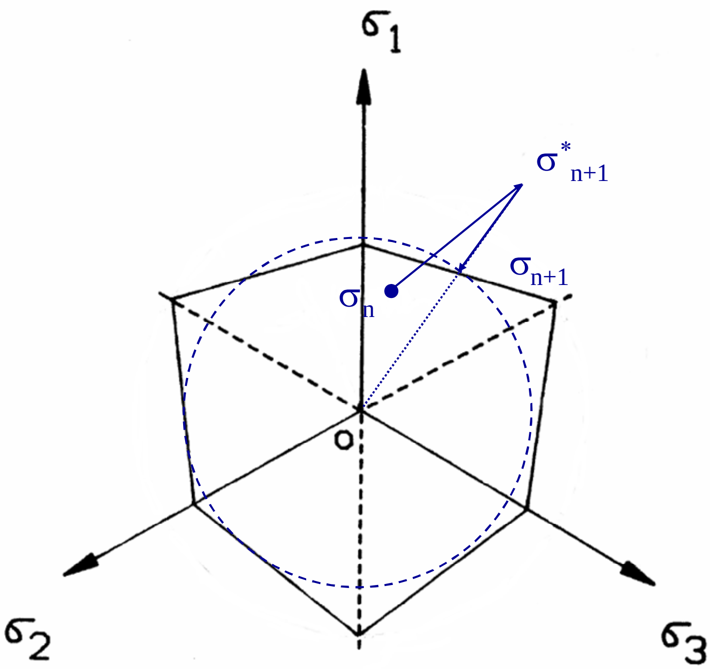

Figure 27. Implementation of Mohr-Coulomb model into CTH.

The parameter m that scales the stress deviators to the flow surface (see, for example, Wilkins [29]) is easy to compute from Eqn. (17) by just replacing $\bar{\sigma} = m\bar{\sigma}^*$ and $\sigma_m = \sigma_m^*$ where σ^* is a trial stress found assuming that the body is elastic:

$$m = \frac{c\,\cos\phi - \sigma_m^*\sin\phi}{\bar{\sigma}^*\left(\cos\theta_0 - \dfrac{\sin\theta_0\sin\phi}{\sqrt{3}}\right)} \tag{18}$$

where, again, c is the cohesion of the MC solid and ϕ its friction coefficient.

A shear stress cap τ_{cap} was also implemented in CTH to limit the shear stress the solid can support. Therefore, the actual MC model that was implemented is:

$$\begin{cases} \tau = c + tan(\phi)\sigma_n & \tau \leq \tau_{cap} \\ \tau = \tau_{cap} & \tau > \tau_{cap} \end{cases} \tag{19}$$

where now the material constants are c, cohesion, $\mu = \tan\phi$, friction coefficient, and τ_{cap} is the cap. The scaling factor when $\tau_{max} > \tau_{cap}$ is given by:

$$m = \frac{\tau_{cap}}{\bar{\sigma}^* cos\phi_0} \tag{20}$$

The implementation of the code was thoroughly checked using simple cases where the answer was known analytically, for example, uniaxial strain or uniaxial stress in compression and tension, pure shear, and triaxial compression.

6.3 Long-Rod Penetration Simulations

6.3.1 Introduction

Experience has shown that, similar to metals, there is a limiting shear stress that a brittle material can support. In metals, for example, this limiting stress is the von Mises yield surface. For the Drucker-Prager and Mohr-Coulomb models, this limiting stress is called a cap, i.e., Y_{cap} and τ_{cap}, respectively. A cap was inferred from the data in Fig. 16 for the Drucker-Prager model, and Fig. 17 for the Mohr-Coulomb model. However, before selecting this value, it is instructive to look at the sensitivity of the penetration results for an assumed value for the cap. For each model, a cap is first estimated (as described below), and then simulations using the parameters dervired from the characterization experiments are compared to the ballistic data.

6.3.2 Drucker-Prager Model

Previous work [30] demonstrated that the most important constitutive parameter at high impact velocities is Y_{cap}, i.e., the computational results are fairly insensitive to changes in Y_0 and β at high impact velocities. The highest velocity datum point was not included in the regression fit for u and v_c versus v_p in Ref. [1]. Since we decided to use the highest velocity point to determine Y_{cap}, the regression analyses for u and v_c were redone, and these are shown in Fig. 26. We selected the highest velocity point (2.817 km/s) and conducted a parametric study on the influence of Y_{cap}. Y_{cap} was varied from 1.0 GPa to 2.4 GPa in increments of 0.2 GPa. The results are shown in Fig. 28.

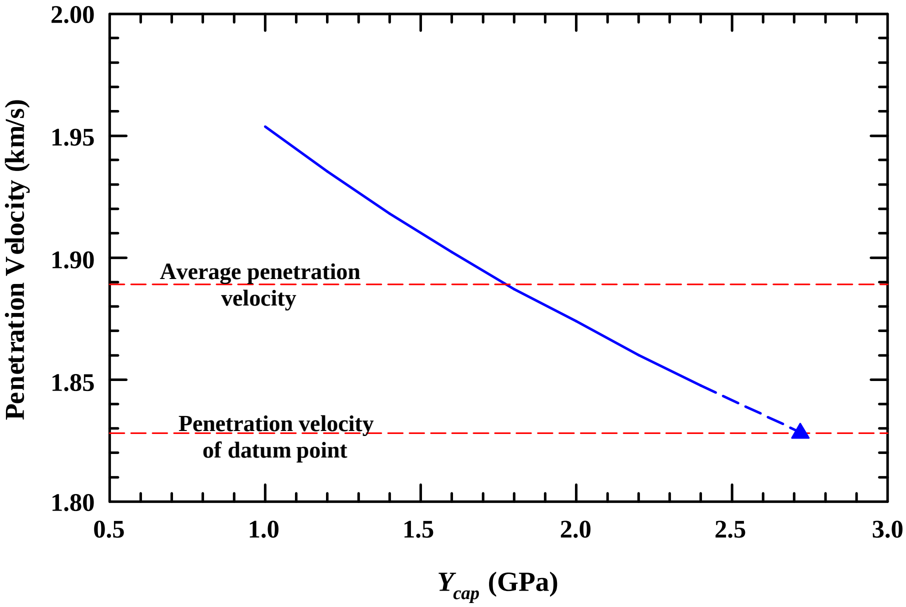

Figure 28. The dependence of the penetration velocity on Y_{cap}.

Two horizontal lines are drawn in Fig. 28: one line represents the penetration velocity for the datum point at 2.817 km/s, while the other represents the least-squares fit of u versus v_p (the dashed line in Fig. 26). The simulation results were extrapolated to the triangular point to estimate Y_{cap} for a penetration velocity of 1.828 km/s. Note that Y_{cap} must be varied considerably to change the penetration velocity from nominally 1.83 km/s (Y_{cap} = 2.72 GPa) to 1.89 km/s (Y_{cap} = 1.78 GPa); Y_{cap} must be decreased by 34% to increase the penetration velocity by 3.3%. In spite of this large variation in Y_{cap}, these values are consistent with an interpretation that confining pressures were sufficiently high in the laboratory tests (Fig. 16) that the cap was achieved.

For the next set of simulations, it was decided that the parameters of the constitutive model should be selected to reproduce the average penetration response, which is represented by the dash line in Fig. 26. The next set of simulations was conducted over the entire range of impact velocities using Eqn. (6) and Y_{cap} = 1.78 GPa. Computational results (not shown) fall significantly below the data at impact velocities less than 1.5 km/s. Examining Table 2, it is observed that β is essentially constant (1.2) for the intact, predamaged, and residual damaged materials; but that Y_0 decreases with increasing levels of damage. We therefore *hypothesize* that the glass in front of the penetrator is more highly damaged than in our laboratory experiments, leading to a lower value of Y_0. Therefore, we conducted a parametric study on Y_0, with $\beta = 1.2$ and Y_{cap} = 1.78 GPa. The impact velocity was incremented in steps of 0.25 km/s, as Y_0 was varied between 0 and 100 MPa. The results are plotted in Fig. 29, where they are compared to the experimental data. The dashed-dot line represents the least-squares regression—as shown in Fig. 26—through the experimental data. It is seen that a value of 25 MPa $\leq Y_0 \leq$ 50 MPa reproduces the penetration velocity quite well for the lower impact velocities. Y_0 is thus taken as an average of 25 and 50 MPa, *i.e.*, Y_0 = 38 MPa.

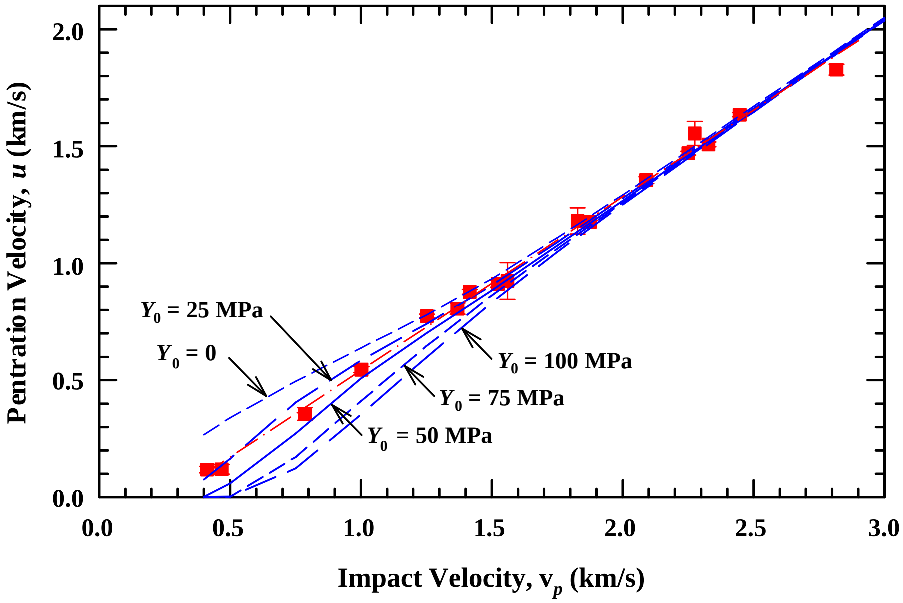

Figure 29. Sensitivity study on Y_0 (with $\beta = 1.2$ and Y_{cap} = 1.78 GPa).

As already indicated, the penetration velocity is not particularly sensitive to changes in Y_{cap}. The simulations indicate that the cap could be between 1.78 GPa and 2.72 GPa (the triangle in Fig. 28); whereas the experimental data indicate that the cap is 2.1 ± 0.2 GPa. We therefore use the experimental data in Fig. 16 to provide the estimate for the cap. However, simulations are required to estimate Y_0 for comminuted glass. Thus, for highly damaged borosilicate glass, the applicable DP constants are:

$$Y = \begin{cases} 0.038 + 1.2P & P \le 1.72\text{ GPa} \\ 2.1\text{ GPa} & P > 1.72\text{ GPa} \end{cases} \qquad (21)$$

where all units are in GPa.

Penetration versus time is nonlinear for the lowest impact velocities [1]. The penetration-time simulation results, using 25 MPa for Y_0, are compared to the experimental data for the experiments conducted at 0.787 km/s and 1.00 km/s in Fig. 30. The experimental data points are linked by the dotted lines. The solid lines are the computational results, and they clearly overpredict the depth of penetration. However, the late time (> ~20 µs) penetration velocity (the slope in Fig. 30) is captured quite-well by the simulations, as indicated by the dashed lines, which are drawn with the same slopes as the solid lines. There is slight nonlinearity of the penetration-time data at early times for v_p = 1.2 km/s, but by 1.5 km/s, the penetration-time curves are linear (i.e., constant penetration velocity). Thus, *it is concluded that at the lowest impact velocities, the assumption that the gold rod penetrates only highly damaged glass is probably not valid; that is, details of the transition from intact to damaged glass appear to be important and cannot be ignored during the early stage of penetration at low impact velocities.*

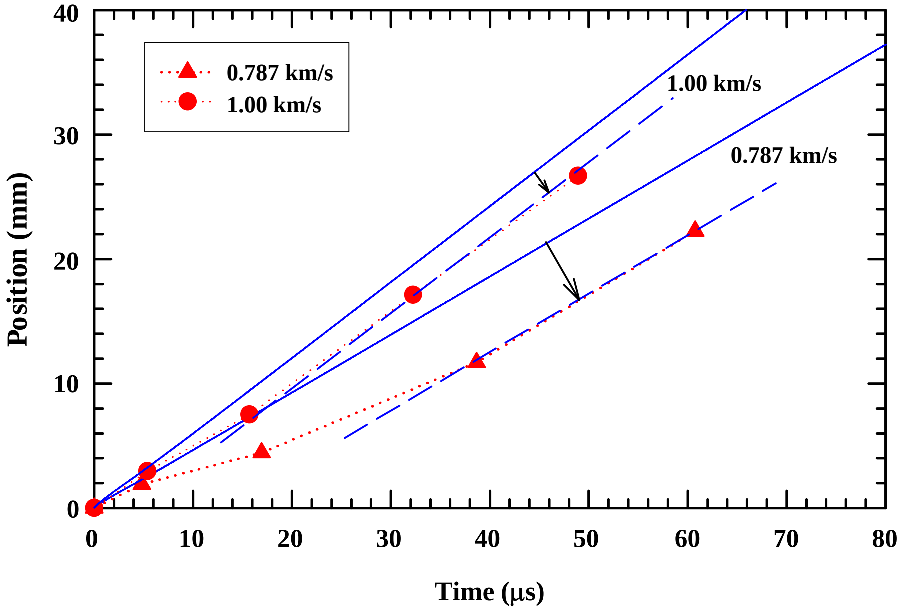

Figure 30. Comparison of the simulation results to position-time data (Y_0 = 25 MPa).

6.3.3 Mohr-Coulomb Model

As mentioned above, the MC model was implemented into CTH. For the first set of simulations, constitutive parameters very similar to the ones obtained in the bomb tests for predamaged specimens were used (a two-parameter model, Eqn. 10). It was found that the penetration velocity was greatly underestimated unless the friction angles and cohesion were greatly reduced. A mesh sensitivity study was conducted, varying the number of zones resolving the projectile radius between 5 (coarse) and 15 (very fine) zones; the simulation results showed very little sensitivity to changes in zoning. Thus, the numerical simulations are numerically resolved.

Therefore, we went to a 3-parameter model by imposing a cap on the shear stress, τ_{cap}. In general, there is not a one-to-one correspondence between DP and MC constitutive parameters. However, for a cylindrical triaxial test where there is radial confinement along with an axial load, then the following equation applies:

$$\tau_{cap} = \frac{Y_{cap}}{2} \tag{22}$$

The conditions of cylindrical triaxiality are reasonably reproduced immediately beneath the penetrating projectile, so Eqn. (22) should approximately hold. A parametric study on τ_{cap} was conducted, similar to the one that was done for Y_{cap} (Fig. 28), using the MC model, at an impact velocity of 2.817 km/s. The results are shown in Fig. 31. We see the same sensitivity between τ_{cap} and the penetration velocity as was shown for Y_{cap}. The results of the parametric study are extrapolated to the penetration velocity of the datum point, represented by the triangle. Again, we elect to model the average penetration response, which from Fig. 31 gives a value of τ_{cap} = 0.925 GPa. This is within 4% of the prediction from Eqn. (21) using Y_{cap} = 1.78 GPa. Given the accuracy of the simulations (particularly in estimating the penetration velocities), we can state that Eqn. (22) provides a relationship between the caps of the DP and MC models in ballistic penetration.

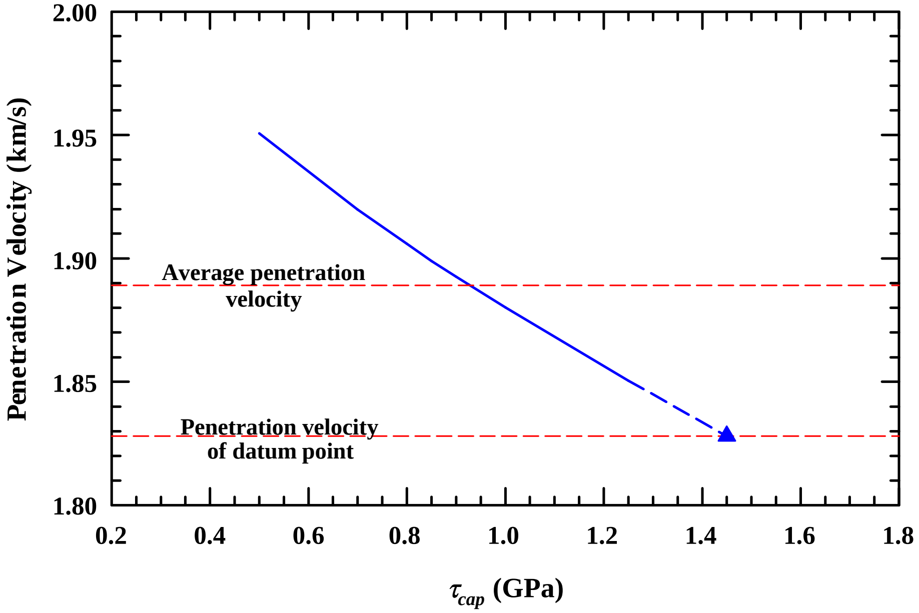

Figure 31. The dependence of the penetration velocity on τ_{cap}.

Next, a parametric study was conducted on the cohesion, c, with μ = 0.6 and τ_{cap} =0.925 GPa. Results are shown in Fig. 32. The numerical results look essentially identical to the results using the DP model, Fig. 29. The cohesion c in the MC model is analogous to Y_0 in the DP model. The fact that numerical simulations need a very small cohesion value to match the ballistic experiments is not seen as a contradiction with the characterization tests. As discussed when the bomb tests were presented, the cohesion decreases with damage. The cohesion of the "residual-strength" material, see Table 3 is already small and, presumably, the material under the projectile is more damaged than the "residual-strength" material tested in the bomb.

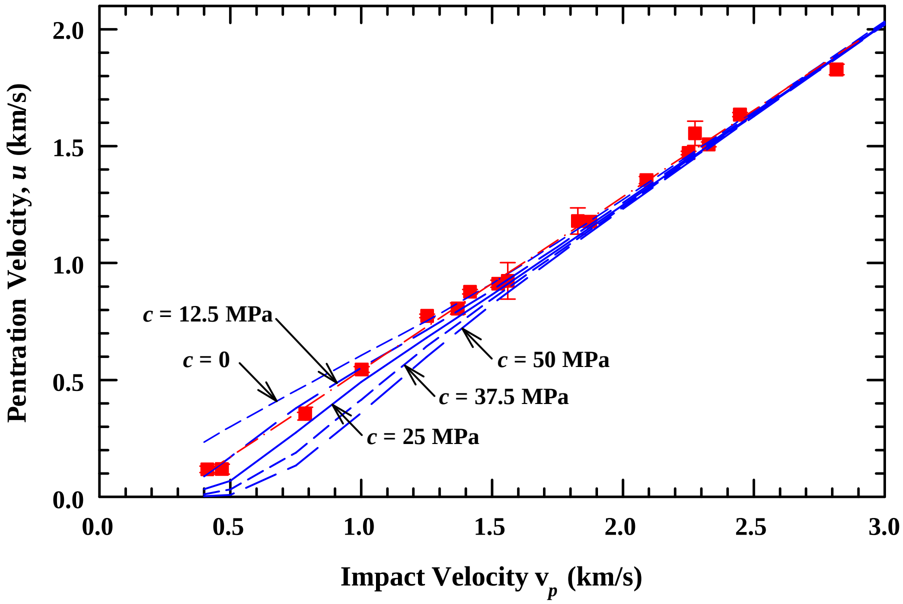

Figure 32. Sensitivity study on c (with $\mu = 0.6$ and $\tau_{cap} = 0.925$ GPa).

Not shown is a graph for the MC model analagous to Fig. 30. The same observations and conclusions hold for the MC model as for the DP model concerning early-time penetration at the lower impact velocities.

Similar to Y_{cap}, it was decided to estimate τ_{cap} from the experimental data instead of taking the value from an "exact" match of the simulations. Given the above considerations, the three parameter MC model proposed for highly damaged borosilicate glass is:

$$\text{Mohr-Coulomb:} \quad \tau = \begin{cases} 0.012 + 0.6\tilde{\sigma}_n & \tilde{\sigma}_n \le 1.65\ \text{GPa} \\ 1.0\ \text{GPa} & \tilde{\sigma}_n > 1.65\ \text{GPa} \end{cases} \tag{23}$$

This model reproduces the characterization experiments (stresses and failure pattern), and the ballistic tests (penetration velocity), although the cohesion needs to be increased substantially for the characterization experiments (see Table 3).

7.0 Characterization Data and Flyer-Plate Impact Data

7.1 Introduction

Borosilicate and soda-lime glass have been the object of extensive plate impact characterization since the pioneering work by Cagnoux [31], Rasorenov, *et al.* [32], and Rosenberg, *et al.* [33]. Of particular interest for our discussion are the papers where the strength of both intact and damaged glass under confinement is presented. Brar, *et al.* [34], as early as in 1991 estimated ≈ 2 GPa as the strength of damaged soda-lime glass at pressures of 4 to 6 GPa. Bourne, *et al.* [9, 35], showed tests with strength values of ≈1.8 GPa for damaged borosilicate and soda-lime for pressures from 4 to 8 GPa. Recently Alexander, *et al.* [10], presented Hugoniot Elastic Limit (HEL) and equation of state data for borosilicate and soda-lime glass. The flyer-plate impact data greatly extends the confining pressures that can be achieved with the hydraulic bomb and confining sleeve techniques. Therefore, we will summarize the results of Bourne, *et al.*, and Alexander, *et al.*, and then provide comparisons between these data and our data.

7.2 Plate-Impact Experiments

The flyer-plate data from Bourne, *et al.* [9,35], and the HEL from Alexander, *et al.* [10], are shown in Fig. 33. In this figure, the black squares are soda-lime glass, the white triangles are borosilicate (Pyrex) glass, and the circle is borosilicate (Borofloat 33) glass. Some explanation of the Bourne, *et al.*, data is required.[4] Bourne, *et al.*, used lateral and longitudinal gauges to measure the stresses in the glass specimens. As they increased the impact velocity, the lateral stress shows a second increase, which is interpreted as the arrival of a failure front [9,35], which lowers the strength. The arrival of the second increase in the lateral stress corresponds to the arrival of a longitudinal recompression wave observed in a VISAR signal in the experiments by Rasorenov, *et al.* [32].

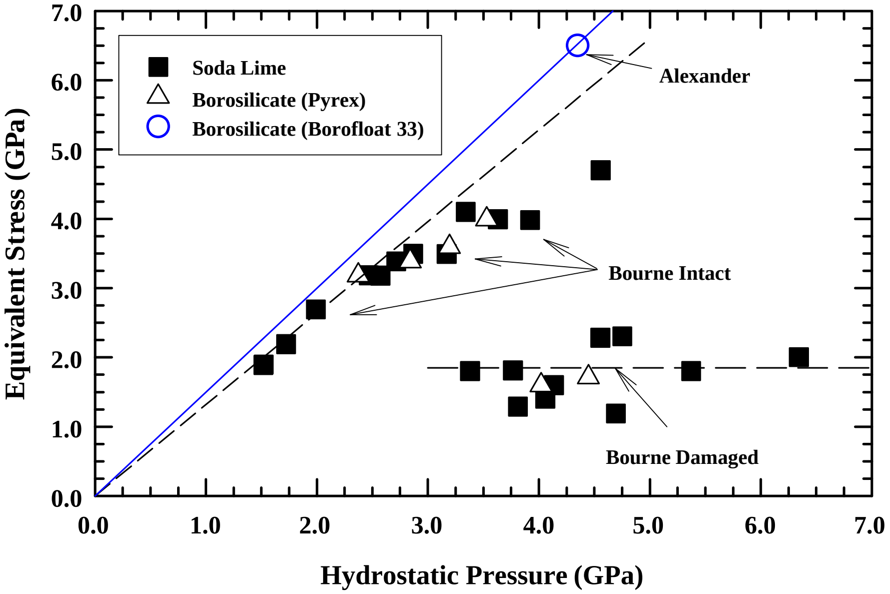

Figure 33. Equivalent stress vs. hydrostatic pressure for flyer-plate impact.

---

[4] Bourne, *et al.* [9, 35], show uncertainty ("error") bars of approximately 0.5 GPa centered on their data values. For clarity, we have omitted these error bars.

The equivalent stress, for uniaxial strain conditions, is $\sigma_{eq} = \sigma_x - \sigma_y$, where σ_y is the lateral stress. The pressure (P), for these uniaxial strain experiments, is given by[5]:

$$P = \frac{1}{3}\left(\sigma_x + 2\sigma_y\right) \tag{24}$$

and the lateral stress is related to the longitudinal stress through Poisson's ratio, ν:

$$\sigma_y = \frac{\nu}{1-\nu}\sigma_x \tag{25}$$

Using Eqn. (25), the equivalent stress is related to the longitudinal stress by:

$$\sigma_{eq} = \sigma_x - \sigma_y = \frac{1-2\nu}{1-\nu}\sigma_x \tag{26}$$

Bourne, *et al.*, [9] use the lowest value of σ_x (the longitudinal stress) where there is a jump in the lateral stress guage (the arrival of the failure wave) to obtain an estimate of the HEL.[6] The long dashed horizontal line through the damaged material in Fig. 33 is σ_{eq} = 1.85 GPa, an average of the strength of the damaged glass. Letting the symbol σ_{fail} represent the dashed line (i.e., 1.85 GPa), then the lateral stress is given by (since $\sigma_{eq} = \sigma_x - \sigma_y = \sigma_{fail}$):

$$\text{Failed Material:}\quad \sigma_y = \sigma_x - \sigma_{fail} \tag{27}$$

Then, inserting Eqn. (27) into Eqn. (24) and solving for the longitudinal stress gives:

$$\text{Failed Material:}\quad \sigma_x = P + \frac{2}{3}\sigma_{fail} \tag{28}$$

Thus, the estimate for the HEL of soda-lime glass is ~4.5 GPa (P = ~3.25 GPa) and that for Pyrex is ~5.2 GPa (P = ~4.0 GPa). It is noted that this value for the HEL for Pyrex is less than the 8 GPa reported in Table 1 of Ref. [35].

The slope of the elastic response in a σ_{eq} versus P graph is derived by manipulations of Eqns. (24-26):

$$\sigma_{eq} = \sigma_x - \sigma_y = 3\left(\frac{1-2\nu}{1+\nu}\right)P \tag{29}$$

Bourne, *et al.*, report that ν for soda-lime glass is 0.23, giving a slope, by Eqn. (29), of 1.32, which is plotted as the short dashed line in Fig. 33. Bourne, *et al.*'s soda-lime glass data fall on this line up to σ_{eq} of approximately 3 GPa, at which point the data begin to deviate from the line. The first Pyrex datum also lies on the short dashed line, and not the solid line, even though Bourne, *et al.*, report that ν = 0.20 for Pyrex [35]. We will return to this observation later.

Alexander, *et al*. [10], determined that the HEL for Borofloat 33—defined as the point where the stress-particle velocity loading path is no longer linear, i.e., the elastic limit—to be 8.7 GPa. By Eqn. (26), this gives a value of 6.5 GPa for the equivalent stress (with ν = 0.20, from Table 1). The corresponding pressure of 4.35 GPa is calculated from:

$$P = \frac{1}{3}\left(\frac{1+\nu}{1-\nu}\right)\sigma_{\text{HEL}} \tag{30}$$

---

[5] For convenience, for this discussion of flyer-plate impact, we assume that the stress is positive in compression.

[6] Presumably, the glass remains elastic below the HEL, but fails upon reaching the HEL.

This point is plotted as the open circle in Fig. 33. The elastic slope, from Eqn. (29) is 1.5, denoted by the solid line in Fig. 33. The solid line goes throught the HEL for Borofloat 33; i.e., the load path is elastic until the HEL. However, an elastic analysis has been assumed, i.e., the bulk modulus and shear modulus—and equivalently, Poisson's ratio—are assumed constant. That is, the fact that the solid line goes through the data point is a statement of self-consistency of the assumption of perfectly elastic response.

A couple of interpretations will be explored in the paragraphs below. As already indicated Bourne, *et al.*'s, data lie on the dashed line ($\nu = 0.23$) until approximately $\sigma_{eq} = 3.0$ GPa ($P =$ ~2.5 GPa), and above this stress, the data lie below the dashed line. This suggests that soda-lime glass is no longer responding elastically. Additionally, the Pyrex data deviate considerably from the $\nu = 0.23$ line (and lie below the $\nu = 0.20$ line), also suggesting that the Pyrex is not responding elastically. This could, perhaps, mean that the glass Bourne, *et al.*, were testing had some predamage, caused by the placement of the lateral stress gages. This also would explain why a value of the Pyrex HEL, which Bourne, *et al.*, inferred from their data, is substantially lower than that determined by Alexander, *et al.* [10].

However, there is another possible explanation/interpretation of the data. The data in Fig. 33 are reploted in Fig. 34. But here, Alexander, *et al.*'s data point has been adjusted to reflect a softening of the bulk and shear moduli, as determined by Holmquist [36], based on volumetric strain data from Alexander [37] and a hydrostat for borosilicate glass by Holmquist [36] based on data from Cagnoux [31]. The hydrostat indicates that there is a softening of the bulk modulus and shear modulus. This "adjusted" data point is more in line with a nonlinear envelope that passes through the Bourne data. But, as will be discussed in the next section, this does not satisfactorily explain inconsistencies between the Bourne data and the characterization data.

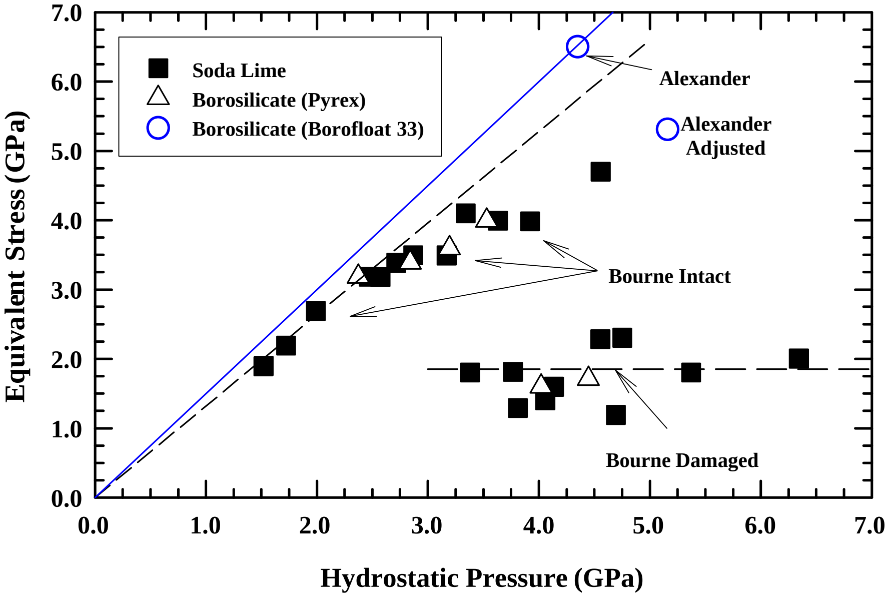

Figure 34. Equivalent stress vs. hydrostatic pressure for flyer-plate impact experiments with adjusted HEL for Borofloat.

7.3 Comparison of Characterization Experiments with Flyer-Plate Impact Experiments

7.3.1 Confined Compression Tests on Intact Borosilicate Glass

The data in Fig. 33 are replotted in Fig. 35, but with the confined compression tests from the hydraulic bomb (open diamonds) and the confined sleeve (inverted open triangles) characterization tests, as well as the unconfined compression tests (open hexagons). An important distinction between these data and the flyer-plate data is that the characterization tests are used to define a failure surface; whereas some of the responses of the flyer-plate experiments (particularly at the lower pressures) appear to be elastic.

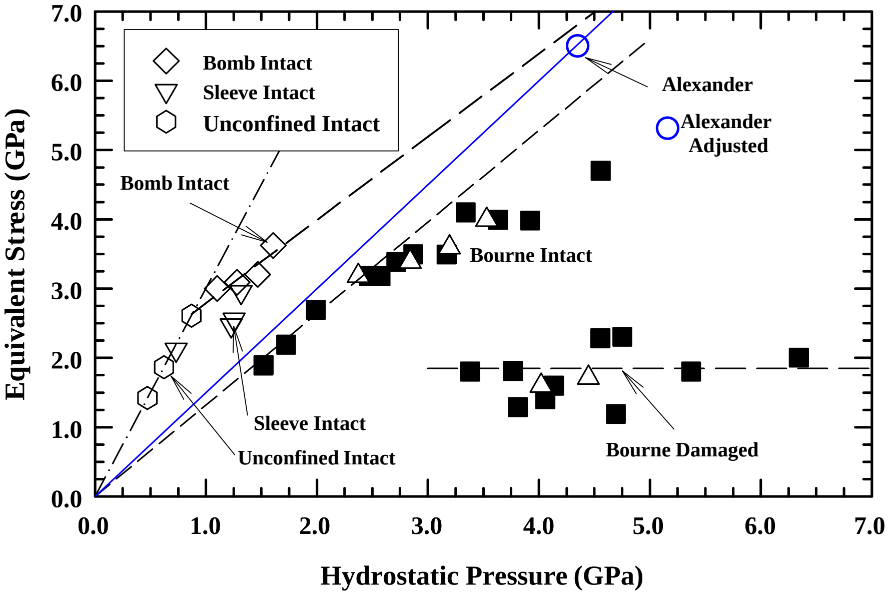

Figure 35. Comparison of intact characterization data with flyer-plate impact data.

A dash-dot line, with a slope of 3, designates the elastic response of an unconfined uniaxial *stress* specimen (σ_x = axial stress; $\sigma_y = \sigma_z = 0$; and $P = [\sigma_x + \sigma_y + \sigma_z]/3 = \sigma_x/3$). The three hexagon data points fall on this curve. These points are plotted where the specimens failed. As mentioned previously, unconfined tests on brittle materials have large scatter in their compressive strengths.

Note that only one of the intact confined sleeve tests lies within the intact data from the hydraulic bomb. We believe that the confined sleeve intact data are not fully reliable for estimating the failure envelope because a small gap, or slight misalignment, between the intact specimen and the sleeve can make a large difference in the confinement pressure and hence the strength. Indeed, the one test, at a pressure of 0.73 GPa lies on the dash-dot line; thus, it failed as if it was an unconfined uniaxial compression test; i.e., the glass failed before it contacted the confining sleeve. In principle, the confined sleeve test should be able to achieve higher confining pressures than the hydraulic bomb test. But in practice, for intact material, this probably can only be achieved if the sleeve was heat shrunk onto the specimen.

However, the hydraulic bomb tests provide very reliable failure data as a function of hydrostatic pressure. The long dashed line through the data is given by Eqn. (5); also see Table 2. Note that as the failure envelope is extrapolated to high pressures, it runs almost through the "elastic" datum point from Alexander, *et al.* [10], but not the adjusted datum point.

With respect to the hydraulic bomb data, it can be argued that there is no requirement for the extrapolation of the failure surface to be linear with pressure. This failure surface could easily have some curvature and go through Alexander's adjusted point; however, much of Bourne, *et al.*'s data lie below the strengths determined form the hydraulic bomb tests, and thus lie below a smooth envelope that would pass through the hydraulic bomb data and the adjusted Alexander data point.

7.3.2 Predamaged Compression Tests on Borosilicate Glass

The ambiguities that exist in interpretation of the intact data do not seem to be evident in a comparison of the predamaged compression data and damaged flyer-plate data. The characterization data from the hydraulic bomb (open large squares) and the confined sleeve experiments (open small squares) are plotted with the other data in Fig. 36 (for clarity, the intact confined sleeve data are not plotted). The hydraulic bomb and confined sleeve data are triaxial tests; thus, the data fall between the uniaxial stress loading path (the dash-dot line) and the uniaxial strain line (the solid line).

The hydraulic bomb data and the confined sleeve data are seen to overlap in pressure, and where they overlap, the equivalent stresses as a function of pressure are in agreement. Much higher confining pressures, and hence hydrostatic pressures, can be achieved with the confined sleeve experimental technique. As observed in Fig. 16, the confining pressures achieved were sufficiently high to observe a maximum stress that can be carried by the damage material. This is denoted by the short dashed line in Fig. 36. This cap is in very good agreement with the cap observed in the Bourne, *et al.*, data. The two lines differ by only ~12% (1.85 GPa versus 2.1 GPa). The difference between these two values lies within the scatter of the experimental data.

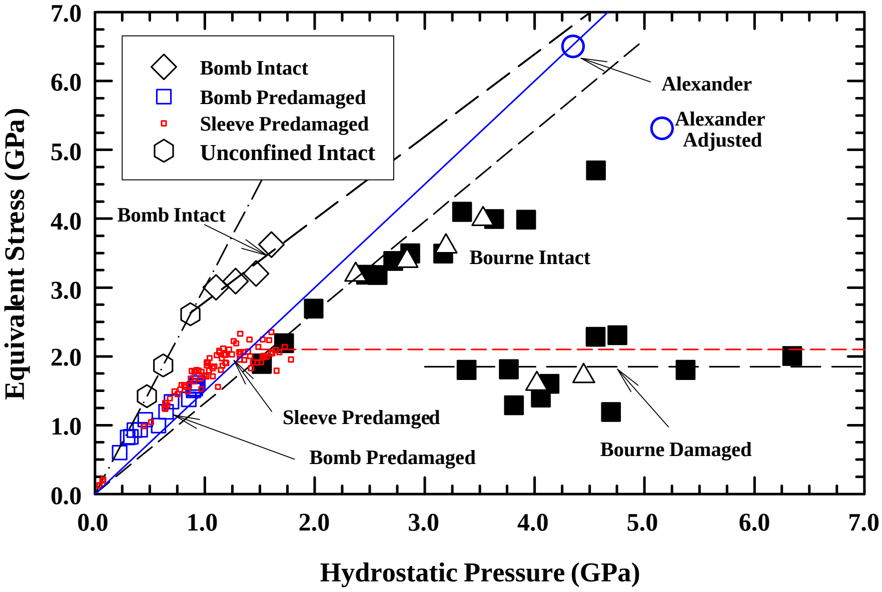

Figure 36. Comparison of predamaged characterization data with flyer-plate impact experiments.

There are several significant conclusions resulting from a comparison of the data in Fig. 36: 1) there exists a maximum load carrying capability, i.e., a cap, for the damaged glass; 2) the failure surface for the damaged glass is independent of strain rate; and 3) there is not any significant decrease in the value of the cap as a function of damage. This last conclusion results from the observation that a cap generated from the quasi-static laboratory experiments does not decrease as a result of further load-reload cycling (and hence, comminution) of the glass during testing; and from the flyer-plate experiments, which presumably, result in a very high degree of damage.

7.3.3 Mohr-Coulomb Representation

The data in Figs. 34-36 are plotted in as σ_{eq} versus P, which is convenient for representing the experimental results in terms of a Drucker-Prager model. These data can be readily converted to a Mohr-Coulomb representation by the following expressions:

$$\frac{(\sigma_1+\sigma_3)}{2} = P + \frac{\sigma_{eq}}{6} \tag{31}$$

$$\frac{(\sigma_1-\sigma_3)}{2} = \frac{\sigma_{eq}}{2} \tag{32}$$

The results are shown in Fig. 37. As before, the solid squares represent the flyer-plate results from Bourne, *et al.* [9,35] for soda-lime glass and the open triangles represent the Bourne data for Pyrex. The open circles represent the HEL as determined by Alexander, *et al.* [10], assuming perfect elasticity, and then adjusted assuming a softening of the bulk and shear moduli [36].

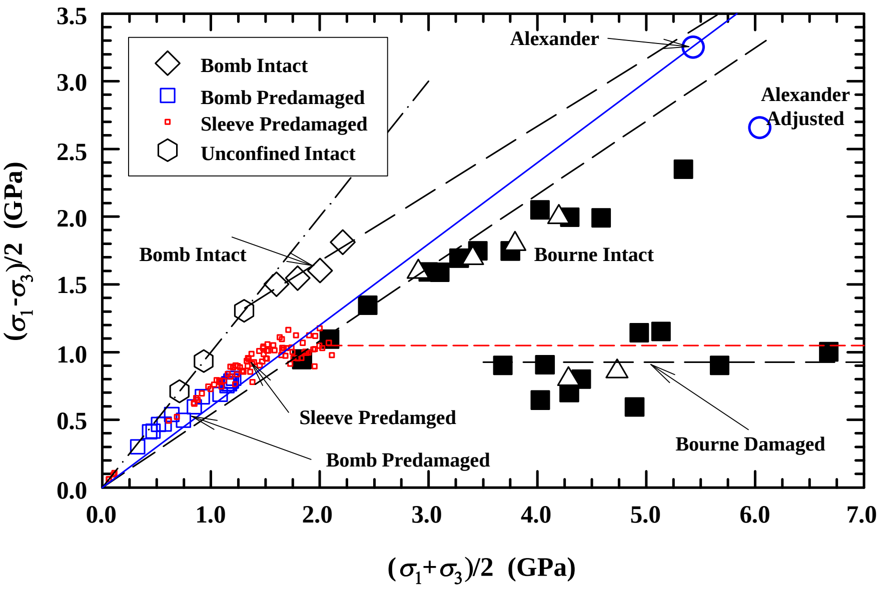

Figure 37. Mohr-Coulomb representation of a comparison of characterization experiments and flyer-plate impact experiments.

8.0 Summary

Laboratory characterization experiments were conducted to gather experimental data that could be used for developing a numerical constitutive model for borosilicate glass that was applicable to ballistic experiments. The strength of glass is pressure dependent, so the characterization experiments were devised to explore the strength of the glass as a function of confining pressure. Interest was in both intact and damaged glass since simulations require a description of both intact and failed material. Three types of characterization experiments were conducted:

- Unconfined compression on intact specimens (uniaxial stress experiments);
- Hydraulic compression using the hydraulic bomb apparatus (triaxial compression, giving equivalent stress versus confinement or hydrostatic pressure) on intact and predamaged specimens;
- Confined sleeve compression experiments (triaxial compression, where the confining pressure increases with axial load) on intact and predamaged specimens.

The focus of the characterization experiments was largely on the latter two test procedures, with the objective of developing failure maps, as a function of pressure, for intact and predamaged material. The confined sleeve test, in principle, can explore higher pressures than possible with the hydraulic bomb test. However, for intact material, small gaps and/or misalignment of the specimen with the sleeve typically resulted in glass failure before full potential confinement could be exerted by the steel sleeve. However, the confined sleeve test worked very well for predamaged specimens, and higher confinement pressures were achieved. The results for the hydraulic bomb and the confined sleeve overlaped at pressures of about 350 MPa, providing increased confidence in the results.

The experimental data were interpreted in terms of two pressure-dependent constitutive models, the Drucker-Prager (DP) model and the Mohr-Coulomb (MC) model. Constitutive parameters were determined from the characterization experiments. The slope (β) for the DP model and the friction angle (ϕ) for borosilicate glass, determined from the characterization experiments, were found to be nominally independent of the degree of damage to the glass (intact, predamaged, residual damage). However, the zero-pressure strength (Y_0) and the cohesion (c) for the DP and MC models, respectively, depended upon the degree of damage, with these parameters decreasing as damage increased. Additionally, the confining pressures in the confined sleeve experiments were sufficiently high to achieve a saturation of the load-carrying ability of the damaged glass, i.e., a cap.

The data from the characterization experiments were compared with flyer-plate impact experiments conducted on borosilicate and soda-lime glass. There appear to be some inconsistencies between the results of the characterization experiments and flyer-plate impact experiments for intact material. However, the equivalent stress derived for failed glass from the flyer-plate impact experiments is in very good agreement with the cap determined for damaged glass from the characterization experiments. This agreement over many orders of magnitude in strain rate shows that a cap exists for damaged (failed) glass, and that this cap is strain rate independent.

The results of the characterization experiments were used to simulate long gold rods impacting borosilicate glass cylinders over a range of impact velocities. The impact experiments had been completed previously [1]. Previous work [30] demonstrated that the cap controls the penetration velocity at high impact velocities, so parametric simulations were conducted to investigate the dependence of the penetration velocity on the cap (Y_{cap} and τ_{cap}). The parametric studies here show that the penetration velocity of an Au rod into borosilicate glass is relatively insensitive to quite large variations in the value of the cap. A ~40% increase in the cap resulted in only a ~3% decreased in the penetration velocity. Nevertheless, the value deduced for the cap from numerical simulations was in agreement with the experimental characterization results.

It was assumed that the projectile penetrated failed material; thus, details of the transition of intact glass to failed glass were avoided. The rationale for this approach was that the failure front propagates much more rapidly than the projectile penetrates; thus, the projectile penetrates failed material.

Parametric studies were required to deduce the zero-pressure strength (Y_0) and the cohesion (c) for the DP and MC models to reproduce the penetration velocities of the gold rod at the lower impact velocities ($v_p < 1.5$ km/s). The values deduced from the simulations were significantly lower than obtained from the characterization experiments. It was concluded that the material beneath the penetrator is more highly damaged (comminuted) than the damaged glass characterized in the laboratory experiments. The DP and MC constitutive constants for *failed* borosilicate glass are:

$$\text{Drucker-Prager:}\quad Y = \begin{cases} 0.038 + 1.2P & P \le 1.72\ \text{GPa} \\ 2.1\,\text{GPa} & P > 1.72\ \text{GPa} \end{cases} \tag{33}$$

$$\text{Mohr-Coulomb:}\quad \tau = \begin{cases} 0.012 + 0.6\tilde{\sigma}_n & \tilde{\sigma}_n \le 1.65\,\text{GPa} \\ 1.0\ \text{GPa} & \tilde{\sigma}_n > 1.65\,\text{GPa} \end{cases} \tag{34}$$

It was also seen that at the lowest impact velocities the constitutive model underestimates the penetration resistance of the glass at early penetration times; however, the simulations reproduce the later time penetration velocities. This suggests that *details of the transition of intact to damage glass are important at the lower impact velocities, and that a more comprehensive glass model (intact, damage initiation, damage propagation) is required in order to model projectile penetration over the full range of impact velocities*.

At this point, the DP and MC constitutive models do equally well in predicting the penetration response of a gold rod into damaged borosilicate glass. Two of the three constitutive constants (the slope and the cap) required for each model were derived from laboratory characterization experiments, but a third parameter—one that appears to be associated with the degree of damage—had to be inferred from matching simulations to ballistic experiments. These observations could potentially simplify a more comprehensive glass model: *damage seems to affect only the zero-pressure intercept (DP model) or cohesion (MC model) of the glass.* A potential advantage of the Mohr-Coulomb model, which may be more relevant for the intact material, is that the MC model provides a characteristic failure angle due to the third invarient, whereas for the DP model, damage is isotropic.

9.0 Acknowledgement

The authors would like to thank Dr. Doug Templeton from TARDEC for funding this work, and the administrative support provide by Mr. Rick Rickert of TARDEC. Also thanks to the ARL for providing ultrasonic modulus measurements of intact samples. Additionally, the authors thank Mr. Tim Holmquist (Southwest Research Institute) and Mr. Dennis Orphal (International Research Associates) for their review of this report. In particular, we thank Dennis for his very careful reading and his many helpful comments and suggestions.

10.0 References

1. Th. Behner, C. E. Anderson, D. L. Orphal, V. Hohler, M. Moll, and D. W. Templeton. Penetration and failure of lead and borosilicate glass against rod impact. *Int. J. Impact Engng.*, **35**(6): 447-456 (2008).
2. C.S. Desai and H. J. Siriwardane. **Constitutive Laws for Engineering Materials with Emphasis on Geologic Materials.** Prentice-Hall, Englewood Cliffs, NJ (1984).
3. W. Chen and G. Ravichandran. Static and dynamic compressive behavior of aluminum nitride under moderate confinement. *J. Am. Ceram. Soc.*, **79**: 579-584 (1996).
4. W. Chen and G. Ravichandran. Dynamic compressive failure of a glass ceramic under lateral confinement. *J. Mech. Phys. Solids*, **45**: 1303-1328 (1997).
5. Z. Ma and K. Ravi-Chandar. Confined compression: A stable homogeneous deformation for constitutive characterization. *Experimental Mechanics*, **40**(38): 38-45 (2000).
6. J. Lu and G. Ravichandran. Pressure-dependent behavior of $Zr_{41.2}Ti_{13.8}Cu_{12.5}Ni_{10}Be_{22.5}$ bulk metallic glasses. *J. Mater. Res.*, **18**: 2039-2049 (2003).
7. W. Chen and H. Luo. Dynamic compressive responses of intact and damaged ceramics from a single split Hopkinson pressure bar experiment. *Exp. Mech*., **44**(3): 295-299 (2004).
8. P. Forquin, A. Árias, and R. Zaera. An experimental method of measuring the confined compression strength of high-performance concretes to analyse their ballistic behaviour. *J. Physique IV*, **134**: 629-634 (2006).
9. N. K. Bourne, J. C. F. Millet, and J. E. Field. On the strength of shocked glasses. *Proc. R. Soc. Lond. A*, **455**: 1275-1282 (1999).
10. C. S. Alexander, L. C. Chhabildas, W. D. Reinhart, and D. W. Templeton. Changes to the shock response of fused quartz due to glass modification. *Int. J. Impact Engng.*, **35**(12): 1376-1385 (2008).
11. P. Patel and M. Matoya. US Army Research Laboratory, Aberdeen, MD, personal communication (2005).
12. K. A. Dannemann, S. Chocron, A. E. Nicholls, and C. E. Anderson, Jr. Compressive damage development in confined borosilicate glass. *Mat. Sci. and Engng. A - Structures*, **478**: 340-350 (2008).
13. K.A. Dannemann, S. Chocron, A.E. Nicholls, J.D. Walker, and C.E. Anderson, Jr. Compression testing and response of SiC-N ceramics: Intact, damaged and powder. *Ceramic Engineering and Science Proc., Advances in Ceramic Armor, 29th Int. Conf. on Advanced Ceramics and Composites* (J. J. Swab, Ed.), **26**: 109-116; American Ceramic Society (2005).
14. S. Chocron, J. D. Walker, A. E. Nicholls, K. A. Dannemann, and C. E. Anderson, Jr.. Analytical model of the confined compression test used to characterize brittle materials. *J. of Appl. Mech.*, **75**: 021006–1-7 (2008).
15. S. Chocron, K. A. Dannemann, J. D. Walker, A. E. Nicholls, and C. E. Anderson, Jr. Constitutive model for damaged borosilicate glass under confinement. *J. of Amer. Cer. Soc.*, **90**(8): 2549-2555 (2007).
16. D. R. Curran, D. A. Shockey, and J. W. Simons. Mesomechanical constitutive relations for glass and ceramic armor. *32nd Int. Conf. on Advanced Ceramics and Composites*, Daytona Beach, January (2008).
17. S. Timoshenko and J. N. Goodier. **Theory of Elasticity**. Mc. Graw-Hill, New York, first edition, 1951.
18. K.W. Peter. Densification and flow phenomena of glass in indentation experiments. *J. Non-Crystalline Solids*, **5**: 103-115 (1970).

19. F.M. Ernsberger. Mechanical properties of glasses. *J. Non-Crystalline Solids*, **25**: 293-321 (1977).
20. J. Lankford, C. E. Anderson, Jr., A. J. Nagy, J. D. Walker, A. E. Nicholls, and R. A. Page. Inelastic response of confined aluminum oxide under dynamic loading conditions. *J. Mat. Sci.*, **33**(6): 1619-1625 (1998).
21. T. J. Holmquist, G. R. Johnson, D. E. Grady, C. M. Lopatin, and E. S. Hertel Jr. High strain rate properties and constitutive modeling of glass. *Proc. 15th Int. Symp. Ballistics*, Jerusalem, Israel, pp. 237--244 (1995).
22. T. J. Holmquist and G. R. Johnson. The failed strength of ceramics subjected to high-velocity impact. *J. Appl. Phys.*, **104**(013533):013533-1–11 (2008).
23. D. C. Drucker and W. Prager. Soil Mechanics and plastic analysis of limit design. *Q. Appl. Math*, **10**(2): 157-175 (1952).
24. R.M. Nedderman. **Statics and Kinematics of Granular Materials**. Cambridge University Press, Cambridge, UK (1992).
25. K. A. Dannemann, S. Chocron, A. E. Nicholls, and C. E. Anderson, Jr. An experimental procedure for analyzing the intact to damage transition in glass. To be submitted (2009).
26. J. M. McGlaun, S. L. Thompson, and M. G. Elrick. CTH: A three-dimensional shock wave physics code. *Int. J. Impact Engng.*, **10**(1-4): 351-360 (1990).
27. D. J. Steinberg. Equation of state and strength properties of selected materials. UCRL-MA-106349, Change 1, Lawrence Livermore National Laboratory, Livermore, CA (1996).
28. G. C. Nayak and O. C. Zienkiewicz. Convenient for of stress invariants for plasticity. *J. Struct. Div., Proc. ASCE*, **98**(ST4): 949-954 (1972).
29. Mark L. Wilkins. **Computer Simulation of Dynamic Phenomena.** Springer-Verlag, Berlin Heidelberg (1999).
30. C. E. Anderson, Jr., S. Chocron, and T. Behner. A constitutive model for in-situ comminuted silicon carbide. *J. Amer. Cer. Soc.*, **93**(6): 1280-1286 (2009).
31. J. Cagnoux. Shock-wave compression of a borosilicate glass up to 170 kbar. *Shock Waves in Condensed Matter – 1981* (W. J. Nellis, L. Seaman, and R. A. Graham, Eds.), pp. 392-396, AIP Conf. Proc. 78, AIP, NY (1982).
32. S. V. Rasorenov, G. I. Kanel, and V. E. Fortov. The fracture of glass under high pressure impulsive loading. *High Press. Res*, **6**: 225 (1991).
33. Z. Rosenberg, D. Yaziv, and S. Bless. Spall strength of the shock-loaded glass. *J. Appl. Phys.*, **59**(8): 3249-3251 (1985)
34. N. S. Brar, S. J. Bless, and Z. Rosenberg. Impact-induced failure waves in glass bars and plates. *J. Appl. Phys.*, **59**(26): 3396-3398 (1991).
35. N. Bourne, J. Millett, Z. Rosenberg, and N. Murray. On the shock induced failure of brittle solids. *J. Mech. Phys. Solid*, **46**(10): 1887-1908 (1998).
36. T. J. Holmquist, private communication (2009).
37. C. S. Alexander, private communication with T. J. Holmquist (2009).